Application of Dual-Frequency Millimeter-Wave Doppler Spectra for the Retrieval of Drop Size Distributions and Vertical Air Motion in Rain

JOHN M. FIRDA, STEPHEN M. SEKELSKY, AND ROBERT E. MCINTOSH

Microwave Sensing Remote Laboratory, University of Massachusetts—Amherst, Amherst, Massachusetts

(Manuscript received 3 September 1997, in final form 10 March 1998)

ABSTRACT

Millimeter-wave Doppler spectra obtained from the dual-frequency Cloud Profiling Radar System (CPRS) are used to retrieve both the drop size distribution and the vertical air motion in rain. CPRS obtains collocated spectra at W and Ka bands through a single 1-m-diameter lens antenna. The vertical air motion is determined primarily from the 95-GHz Mie scattering from rain, whereas turbulence effects are minimized by correlating the drop size distributions measured at both the 95- and 33-GHz frequencies. The authors describe an iterative procedure that estimates the drop sizes and vertical motions with range and horizontal resolution of 60 m and temporal resolution of 2 s. Model drop size distributions are used to initiate the procedure, but the retrieved distributions and vertical air motions are seen to be independent of the particular model used.

Data were gathered to test the procedure during the Ground-Based Remote Sensing Intensive Observation Period (GBRS IOP) sponsored by the Department of Energy Atmospheric Radiation Measurement (DOE ARM) program. The measurements represent the first simultaneous Doppler spectra of rain at these frequencies. The experiment took place in April 1995 at the Cloud and Radiation Testbed (CART) site in Lamont, Oklahoma. Radiosonde and surface measurements of temperature and pressure were used in the retrieval algorithm. Rain events from stratiform and transition region (i.e., decaying from the convective region toward the stratiform region of a storm) clouds were observed and are analyzed in this paper. The rain rate for the stratiform rain case was relatively uniform with small amounts of vertical air motion. Variations of the vertical winds for the transition region case, however, were larger and more frequent and were accompanied by short intense downbursts. The algorithm's results are best for rain rates higher than 1 mm h^{-1}.

1. Introduction

Research into the drop size distribution of rain clarifies the inner processes of rain development. By quantifying the total amount of liquid flux in the atmosphere, it also extends our knowledge of the ice clouds above the melting layer. In addition, several parameters can be accurately calculated, which can then be used to verify theoretical equations for attenuation, liquid water content, and the like.

Several researchers have attempted the remote retrieval of drop size distributions aloft in rain using ground-based, vertically oriented Doppler radar spectra measurements (Rogers and Pilié 1962; Battan and Theiss 1966; Caton 1966; Sekhon and Srivastava 1971; Hauser and Amayenc 1981). The Doppler spectrum method relates drop size to terminal velocity, assuming a unique relationship exists between the two. Unfortunately, it is impossible to independently measure the vertical air motion from the terminal velocities of falling drops. The vertical air motion shifts the Doppler spectra along the velocity axis, so errors are included in the retrieved drop size distributions. Spectral broadening from turbulence is another limiting factor in the retrievals.

Extracting the vertical air motion in rain is a useful parameter in itself because this information sheds light on the physical processes within a rain storm. The strength of updrafts and downdrafts can be related to the amount of convection in a storm as well (Doviak and Zrnić 1993). The first approach developed to extract vertical air motion was the lower bound method, which assumes there are a sufficient number of drops of a minimum detectable size associated with a minimum detectable velocity (Probert-Jones and Harper 1961). The minimum detectable velocity can then be compared to the measured spectra to find the error due to vertical air motion. This method suffers from several problems, however (Atlas et al. 1973). First, it assumes a sufficient number of drops are present of some diameter, which may or may not be the case. Second, fading effects create noisy spectral shapes, making it difficult to determine the lowest velocity detected in the presence of noise. Third, the dynamic range of the Doppler spectrum must be large enough to determine the minimum ve-

Corresponding author address: Dr. Steven M. Sekelsky, University of Massachusetts, Knowles 209C, Amherst, MA 01003.
E-mail: sekelsky@mirsl.ecs.umass.edu

locity. And finally, turbulent broadening is not accounted for in detecting the minimum bound.

Subsequently, Rogers (1964) developed a method that assumes a unique relationship between velocity and reflectivity. By using a measurement of reflectivity it predicts the corresponding velocity; the vertical air motion is the difference between the measured and predicted velocities. This method significantly improves on the lower bound method, but errors are typically 1 m s^{-1}, which corresponds to errors of one order of magnitude in the estimated distribution (Atlas et al. 1973).

Hauser and Amayenc (1981) proposed a method called the 3P approach that simultaneously adjusted three parameters to obtain the distribution. It numerically fits simulated Doppler spectra to measured spectra using least mean squares estimation by first varying the vertical air motion and then the slope and offset of an exponential drop size distribution. Although the algorithm produces reasonably good results for stratiform rain, its application is limited because it assumes an exponential drop size distribution, and it only works if turbulence is negligible. In stratiform rain cases the offset parameter can be determined effectively, but the slope and vertical air motion estimates are questionable (Hauser and Amayenc 1984).

During the 1980s, several researchers applied data from wind profilers to obtain drop size information (Wakasugi et al. 1986; Gossard 1988; Gossard et al. 1990; Rogers et al. 1993). Observations of the spectra for low rain rates revealed that the clear-air peak and rain peak are distinguishable some of the time. Therefore, the vertical wind estimate can be used to remove the effects of vertical air motion. This method can work for stratiform rain with low rain rates, but it has limitations. The averaging time of most wind profilers is 30 s or greater. If the rain drops experience both updrafts and downdrafts during this time, the averaged spectra have an artificially induced spread. This is difficult to separate from turbulent broadening, but the presence of turbulence is necessary to receive a strong enough clear-air echo (C_n^2; Tatarskii 1971) for air motion detection. Another problem is that the beamwidth of wind profilers is typically large, approximately 7°, causing more spread in the Doppler spectra. Thus, wind profiler data is limited to drop size retrievals given low rain rates and relatively uniform wind fields.

Other methods estimate vertical winds in rain from velocity–azimuth display (VAD) scans, which collect Doppler data in a conical scan to extract horizontal and vertical winds (Doviak and Zrnić 1993). These methods estimate the average wind over large areas and therefore require fairly uniform wind fields in the resolution volume.

Thus, the above methods work best in situations of uniform wind with small variation in time and negligible effects from turbulence. But to fully understand rain processes, other situations must also be accurately quantified. Millimeter-wave radars have the potential to estimate vertical winds in rain where complex wind fields exist, even in convective situations where changes in wind and drop size distribution occur rapidly. Millimeter waves are highly sensitive to small hydrometeors, allowing radars to acquire data at much higher spatial and time resolution than low-frequency systems. Mie scattering effects observed at millimeter wavelengths for large cloud particles and precipitation provide more information to extract particle size as well. Millimeter waves also offer other practical advantages; they require lower peak powers and antenna sizes so the radar systems can be compact, portable, and easily deployed to remote locations across the globe (Mead et al. 1994).

Lhermitte (1987, 1988) proposed a method that uses the location of the Mie backscattering null seen in 94-GHz Doppler spectra to determine the vertical air motion. This work provides a better criterion to detect vertical air motion, as the null location can be predicted reliably. The algorithm uses correlation analyses between measured and simulated Doppler spectra to remove vertical air motion and turbulent broadening. Results for stratiform rain have been promising, and the method also has potential when turbulence and complex wind fields are present.

This paper presents an algorithm that builds on Lhermitte's method to exploit the Mie scattering effects for vertical wind detection and uses two Doppler spectra to account for broadening terms to solve for the distribution. The vertical air motion estimate is determined iteratively by feeding retrieved drop size distributions back into the algorithm in place of an initial model. Sample results of the algorithm are presented, and the results are qualified with theoretical justification and self-consistency tests.

With two millimeter-wave radars, one can extract the vertical air motion and drop size distribution with high spatial resolution and greater independence from models. The fundamental concept is that while the two Doppler spectra demonstrate differences, the retrieved drop size distributions are frequency independent and will be highly correlated once all corrupting factors are removed. Single-frequency retrieval algorithms typically depend on fitting the measured spectra to a particular model form of the distribution. The use of two millimeter-wave Doppler spectra provides characteristics that can be used to solve for the distribution without having to explicitly fit the Doppler spectra to one model.

The algorithm was tested on data obtained with the Cloud Profiling Radar System (CPRS) (Sekelsky and McIntosh 1996; Lohmeier et al. 1997), a dual-frequency millimeter-wave Doppler radar that collects high-resolution measurements of clouds and precipitation. Collocated data are obtained with a single 1-m lens antenna for transmitted and received signals at both frequencies. The data were gathered during April 1995 at the Ground-Based Remote Sensing Intensive Observation Period (GBRS IOP), a Department of Energy Atmospheric Radiation Measurement (DOE ARM) program–

sponsored experiment. CPRS obtained pulse-pair and Doppler spectra of clouds and precipitation for 3 weeks while stationed at the DOE's Cloud and Radiation Testbed (CART) site in Lamont, Oklahoma.

The organization of this paper is as follows. Section 2 discusses the basic formulation for drop size retrieval using Doppler spectra. It also describes the major problems encountered and then presents the dual-frequency algorithm. Section 3 discusses the GBRS-IOP experiment and provides an overview of the radar system. Section 4 presents specific rain events of interest and discusses the consistency of the results. Section 5 concludes with results of a statistical analysis to determine the algorithm's dependence on the initial drop size model used. Other results are also discussed that indicate the limitations of our procedure.

2. Methodology for drop size retrieval

a. Basic formulation

The Doppler spectrum is a power-weighted measure of a target's backscatter per velocity bin v to $v + dv$, where dv is the velocity resolution (Doviak and Zrnić 1993). It can be related to the drop size distribution $N(D)$ by

$$S(v) = N(D)\,\sigma(D)(dD/dv), \quad (1)$$

where $\sigma(D)$ is the backscatter cross section (mm^2) and dD/dv is a relationship between the target's drop diameter and terminal velocity (mm m^{-1} s). Extracting $N(D)$ from a measured $S(v)$ relies upon knowing the size–backscatter relationship and a unique relationship between terminal velocity and particle size.

In the case of rain, a commonly used distribution is the exponential form given by

$$N(D) = N_o \exp(-aR^bD), \quad (2)$$

where R is the rain rate (mm h^{-1}), D is particle diameter (mm), N_o is a proportionality constant, and a and b are constants that determine the slope of the distribution. An empirically determined form of (2) is the Marshall–Palmer (M–P) drop size distribution where $N_o = 8000$ m^{-3} mm^{-1}, $a = 4.1$, and $b = -0.21$ (Marshall and Palmer 1948). Actual drop size distributions vary significantly from this, however, and other forms of the distribution have been proposed. Of these the gamma distribution (Ulbrich 1983) is commonly applied:

$$N(D) = N_oD^{\mu} \exp(-aR^bD), \quad (3)$$

where μ is an integer from -3 to 8. The exponential form is a special case of the gamma distribution with μ equal to 0.

Retrieving drop size information relies on knowledge of a unique relationship between a target's size and terminal velocity. Gunn and Kinzer (1949) empirically determined this relationship for rain, and several formulas have been fit to the data. Lhermitte (1987, 1988) references the equation

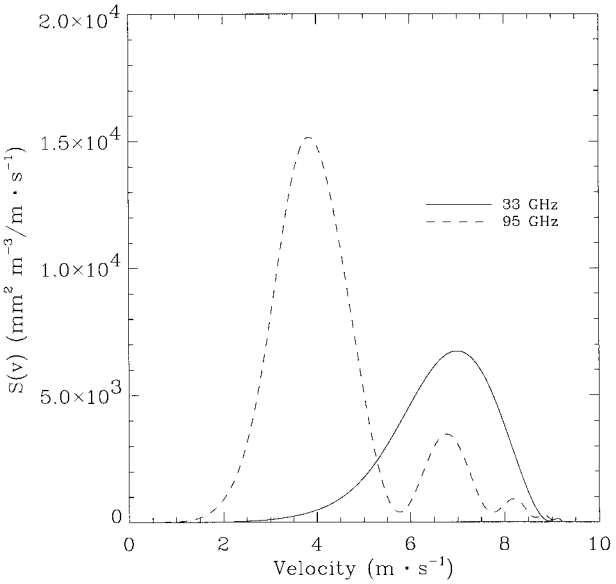

FIG. 1. Simulated Doppler spectra at 33 and 95 GHz using Marshall–Palmer with a 10 mm h^{-1} rain rate.

$$v(D) = 9.25[1 - \exp(-6.8D^2 + 4.88D)], \quad (4)$$

where v is in meters per second and D is in centimeters. The Gunn and Kinzer data was taken at sea level, however, and terminal velocities increase as altitude increases due to the decrease in air density (Foote and duToit 1969). The terminal velocities can be corrected by multiplication with the factor $(\rho_o/\rho)^{0.4}$, where ρ_o is the air density at sea level and ρ is the air density at the altitude of the measurements.

Therefore, given relationships to associate backscatter and terminal velocity to drop size, one can divide a measured spectra by $\sigma(v)$ and dD/dv to extract $N(D)$. However, updrafts, downdrafts (vertical air motion), and the effects of turbulence all bias the measurement. Vertical air motion manifests itself by shifting the spectrum up and down the velocity axis, while turbulence spreads the velocity spectrum. As noted in the introduction, algorithms developed to remove these biases from radar data to extract $N(D)$ have yielded varying results.

b. Dual-frequency method

The dual-frequency method (DF method) is designed around existing algorithms and builds upon strategies to remove biases while exploiting the advantages of Mie scattering. The fundamental premise is that while the shape of the Doppler spectrum is frequency dependent, the drop size distribution is not. Millimeter-wave scattering falls into the Mie resonance region for raindrops providing highly visible differences between the spectra. Consider Fig. 1, which shows simulated Doppler spectra at 33 and 95 GHz for a rain rate of 10 mm h^{-1}. Whereas the 33-GHz spectrum resembles a Gaussian shape, the 95-GHz spectrum contains several nulls and peaks. This

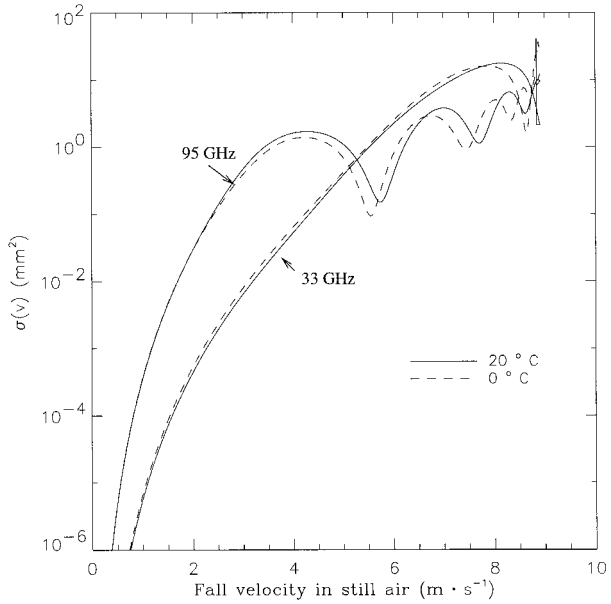

FIG. 2. Mie backscatter cross section as a function of velocity for 33 and 95 GHz at 0° and 20°C calculated at sea level.

can be understood by examining the Mie backscatter equation for spherical water droplets $\sigma(v)$ plotted in Fig. 2 for 0° and 20°C. At 95 GHz, the Mie oscillations are within the fall velocities for rain. These oscillations modulate the Doppler spectrum producing a bimodal spectrum. With collocated measurements at 33 and 95 GHz, the retrieved distributions can be correlated by properly removing biases. An iterative procedure can accomplish this by adjusting the estimates of vertical air motion and turbulence until spectral distributions measured by the two frequencies agree. A flowchart of the algorithm that we use in this paper is shown in Fig. 3.

The first step in the algorithm is to model the Doppler spectrum at the lowest range gate of the first time profile using three parameters. First, the temperature of the water must be specified in order to determine the water's dielectric constant. Figure 2 demonstrates the temperature dependence of the scattering curves for 33 and 95 GHz for 0° and 20°C. The first null location occurs approximately 0.2 m s^{-1} lower for 0° than for 20°C. The temperature and air pressure are also needed for the air density correction factor. Both measurements can be obtained using surface and radiosonde data.

The second consideration is the degree to which the droplets deviate from sphericity. As rain drop size increases, the shape deforms from a sphere to an oblate ellipsoid, then flattens and eventually becomes concave on the bottom for large drops (Doviak and Zrnić 1993). Therefore, the retrieved distribution must be considered in terms of equivolume spheres, meaning the volume of a sphere with a diameter D will be equivalent to the volume of an ellipsoid with major and minor axes a and b, respectively. Each drop diameter is modified according to Green's model for raindrop shape (Green 1975), and the major axis of the ellipsoid is used in the Mie calculation. Note, a more sophisticated scattering curve that accounts for drop shape deformities may be necessary to get accurate $N(D)$ estimates for high rain rates, as the population of large drops increases.

The final parameter is the rain rate, which is related to the equivalent reflectivity factor Z_e through (1) because Z_e is the integration of the Doppler spectrum over all velocity bins:

$$Z_e = \frac{\lambda^4}{|K_w|^2 \pi^5} \int_0^\infty S(v)\, dv, \tag{5}$$

where $|K_w|$ is calculated from the index of refraction of water and λ is the wavelength of the radar. Figure 4a shows equivalent reflectivity factors calculated at 33 and 95 GHz using an M–P drop size distribution and (5) plotted on a dBZ_e scale (i.e., 10 $\log_{10} Z_e$). However, equivalent reflectivity factor measured at millimeter-wave frequencies is invalid until the attenuation between the radar and scattering rain cell is removed. Attenuation is induced through oxygen and water vapor absorption, off-nadir scattering, and absorption from raindrops as the transmitted and reflected signals propagate through the rain. The one-way attenuation rate (dB km^{-1}) can be calculated by integrating a specified extinction cross section and drop size distribution over all drop diameters, according to Doviak and Zrnić (1993) Eq. (3.15):

$$K = 4.34 \times 10^3 \int_0^\infty N(D)\sigma_e(D)\, dD. \tag{6}$$

Here $\sigma_e(D)$ is calculated using Mie formulations for scattering and absorption. Figure 4b shows the extinction rates for 33 and 95 GHz versus rain rate using an M–P drop size distribution at 20°C. The extinction rates are calculated for each range cell and the total attenuation between the radar and a rain cell is obtained by integrating the extinction rates from the ground up to the rain cell. Attenuation must be calculated for each range gate to account for temperature and variations of extinction rates with range.

Once attenuation is removed, rain rate can be determined by comparing equivalent reflectivity factor measurements with a simulation. With two frequencies there is an extra degree of freedom, as the ratio of the equivalent reflectivity factors, commonly known as the dual-wavelength ratio (DWR), increases with rain rate, as shown in Fig. 4c. The DWR is calculated using

$$\text{DWR} = 10 \log_{10}(Z_{e_{33}}/Z_{e_{95}}). \tag{7}$$

The difference between 33- and 95-GHz equivalent reflectivity factors increases with rain rate because Mie resonances affect the scattering cross sections of the drops. If attenuation effects are added, the difference becomes larger, and DWR increases more rapidly with rain rate, as shown in Fig. 4c, which plots DWR with 1 km of two-way attenuation from rain. The rain rate

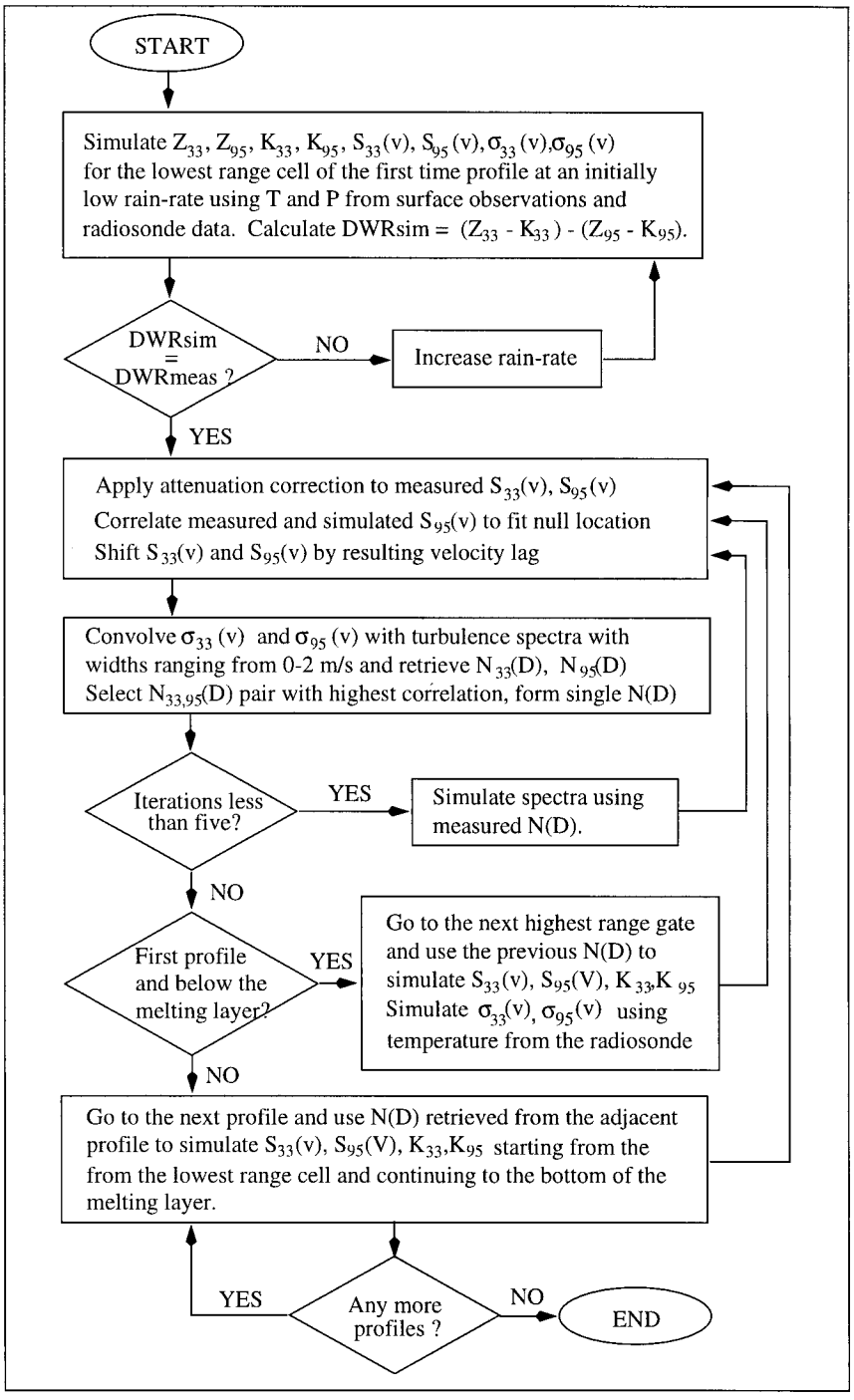

FIG. 3. Flowchart of the dual-frequency drop size distribution retrieval algorithm.

is determined by calculating the attenuated equivalent reflectivity factors from (1), (5), and (6) for increasing rain rates until the simulated DWR is equal to the measurement.

Once a model of the Doppler spectrum is specified, an analysis of the correlation between measured and simulated Doppler spectra provides an initial estimate of vertical air motion (Lhermitte 1987). Consider Fig. 1 again, which shows examples of spectra at the two frequencies. The spectral shapes are preserved in the presence of vertical air motion, as updrafts and downdrafts merely shift the spectra along the velocity axis. To extract the vertical air motion, the measured 95-GHz spectrum is shifted along the velocity axis to find the

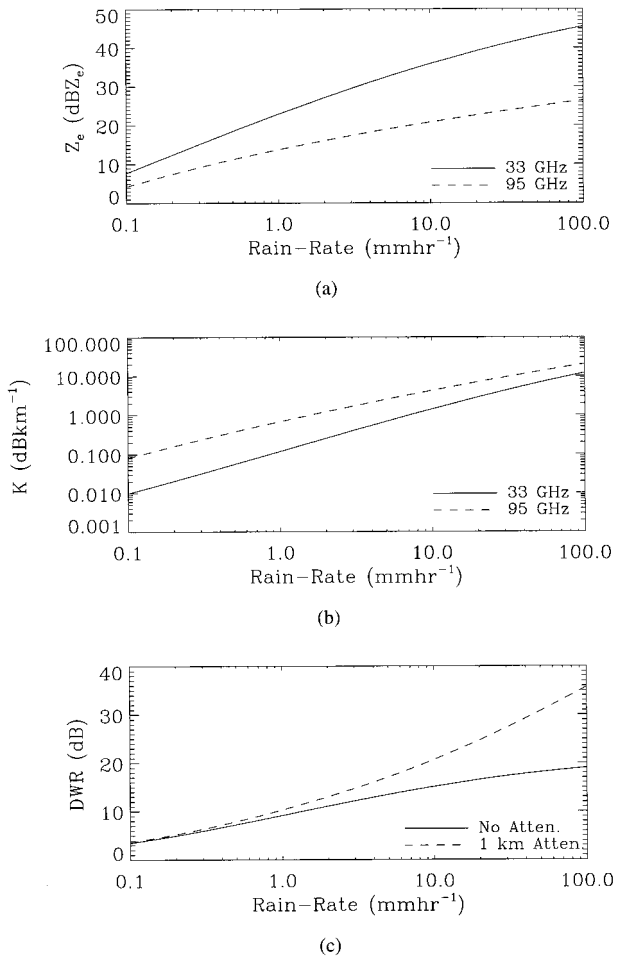

FIG. 4. (a) Equivalent reflectivity factor vs rain rate. (b) Extinction vs rain rate. (c) Dual-wavelength ratio vs rain rate. The solid curve has no attenuation, and the dashed curve includes 1 km (2 way) of attenuation from rain drops using a Marshall–Palmer drop size distribution. All data for (a)–(c) are for 33 and 95 GHz assuming a Marshall–Palmer drop size distribution.

best correlation with the simulation using only the spectral points between the first two peaks. The correlation matches the location of the null, which is dominated by the oscillations in the backscatter equation. It depends weakly on rain rate, but the rain rate must be high enough for the null to be distinguishable (about 1 mm h^{-1} minimum). The Mie backscatter calculations account for its temperature dependence.

The drop size model is only an approximation, and therefore the shapes of simulated Doppler spectra differ among models. These differences are large enough to bias the vertical air motion estimate, however. A closer approximation can be obtained with a retrieved drop size distribution. Once an estimate of the drop size distribution is made, it can be used to simulate another Doppler spectra, which is then correlated to the measured spectra. By performing several iterations of the correlation, the vertical air motion estimate is nudged closer to the actual value, and the dependence on the original model is reduced. The iterations are applied after turbulence is accounted for and a drop size distribution is retrieved using (1).

Turbulence causes a random velocity variation about the mean, resulting in a distribution of particles falling at the same velocity. This spreads the Doppler spectrum and for 95 GHz smoothes the bimodal spectrum and fills in the nulls. Turbulent broadening may be approximated by the convolution of the Doppler spectrum with a Gaussian distribution. Figure 5a shows an example of turbulence where the Doppler spectra for the 10 mm h^{-1} rain-rate case have been convolved with a Gaussian spectrum with a 0.25 m s^{-1} width. Notice that while the null begins to fill in, its position is nearly unaffected, moving by only 0.035 m s^{-1}. Note also that these effects are not as easy to observe for the 33-GHz spectrum and could be confused with effects due to slightly altering the model $N(D)$.

Turbulence can be removed from the measurement by convolving the backscatter equation with a turbulence distribution of appropriate width, chosen by iteratively convolving the simulated Doppler spectra with turbulence distributions of different widths and then correlating it to the measurement to find the best fit (Lhermitte 1987). However, this still depends heavily on the form of the distribution. Having two Doppler spectra with at least one exhibiting Mie effects offers an alternative method. If a Doppler spectrum corrupted with turbulent broadening is divided by the backscatter equation, the oscillations from Mie scattering produce similar oscillations in the retrieved $N(D)$. For example, Fig. 5b shows the spectra from Fig. 5a fed into (1) ignoring turbulence. Notice the humps in the distribution and the diverging results between 33 and 95 GHz. The broadening can be iteratively solved for by convolving the backscatter equations with turbulence spectra of varying widths and applying (1). The resulting $N(D)$s can then be correlated to find the turbulence widths and applying (1). the resulting $N(D)$s can then be correlated to find the turbulence width that produces the closest match between the two frequencies. The final result therefore relies less on the form of the model distribution.

The final step in our algorithm is to form one drop size distribution by averaging the two retrieved distributions. However, the distributions must be weighted by the signal-to-noise ratio at different drop sizes. Consider Fig. 1 once more. Between the two frequencies, both high and low signal-to-noise ratios occur at different drop sizes. Therefore, at each drop diameter the distributions are averaged together and weighted with the signal-to-noise ratio of the measuement such that

$$N(D) = \frac{\mathrm{s/n}_{33}(D)}{\mathrm{s/n}_{33}(D) + \mathrm{s/n}_{95}(D)} N_{33}(D) + \frac{\mathrm{s/n}_{95}(D)}{\mathrm{s/n}_{33}(D) + \mathrm{s/n}_{95}(D)} N_{95}(D), \quad (8)$$

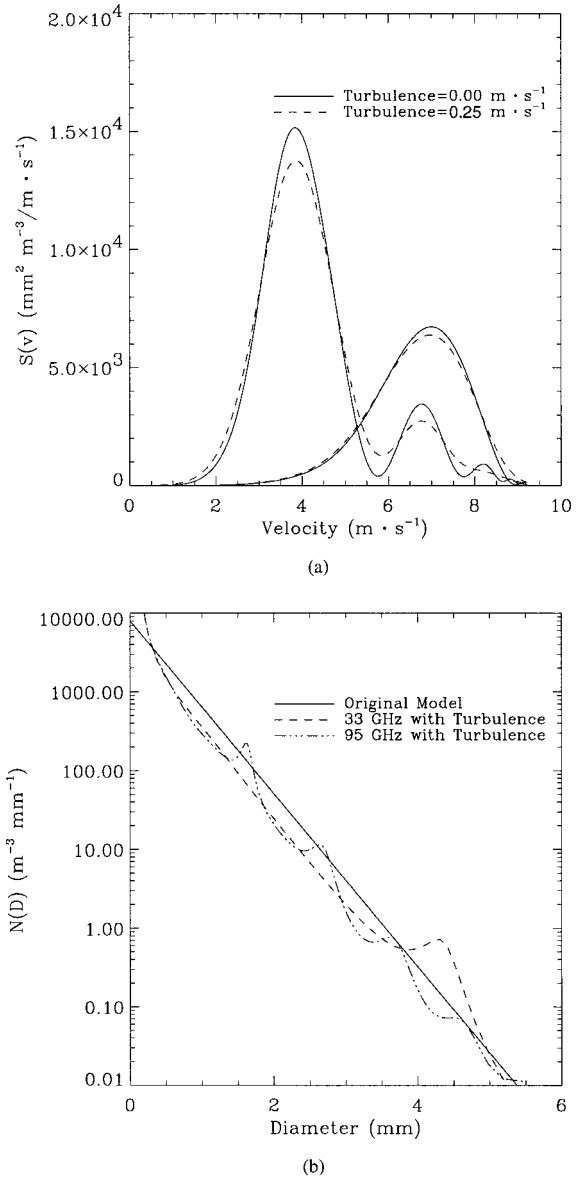

FIG. 5. (a) Simulated Doppler spectra at 33 and 95 GHz using Marshall–Palmer for 10 mm h^{-1} rain rate convolved with 0.25 m s^{-1} wide turbulence spectra. (b) Drop size distributions retrieved from simulated 33 and 95 GHz turbulence corrupted Doppler spectra using Marshall–Palmer with a 10 mm h^{-1} rain rate and a 0.25 m s^{-1} wide turbulence spectra compared with the original $N(D)$.

where D is diameter; $s/n_{33}(D)$ and $s/n_{95}(D)$ are the signal-to-noise ratios for the 33 and 95 GHz at each diameter, respectively; and $N_{33}(D)$ and $N_{95}(D)$ are the drop concentration estimates at each diameter, respectively. Thus, when one of the spectra has a higher signal-to-noise ratio than the other, its distribution is weighted more in the final average distribution. If both spectra fall into the noise, the drop concentration estimate is thresholded to zero.

Once the drop size distribution for the first pixel is retrieved, the adjacent pixels can be analyzed using this distribution in place of a model. The radar measurements have high spatial and temporal resolution, and the variation in the drop size distribution is small from pixel to pixel. Thus, a retrieved drop size distribution from an adjacent pixel will be a closer approximation than a simulated distribution. Therefore, the next range cell uses the distribution retrieved from the previous range cell to calculate attenuation and simulate a Doppler spectra for vertical air motion detection. Turbulence is accounted for in the same way as the first pixel, and the retrieval is iterated to remove any bias from spatial variations.

After all the range cells of the first time profile are analyzed, the second time profile uses distributions from adjacent range cells of the first time profile to calculate attenuation and simulate Doppler spectra for vertical air motion detection. Thus, the lowest range cell in the second time profile starts the retrieval with the lowest range cell in the first time profile, the second range cell in the second time profile starts the retrieval with the second range cell in the first time profile, and similarly to the highest range cell. Then the third profile uses the distributions from the second profile and so on until all the time profiles are analyzed.

c. Self-consistency of the data products

Once the drop size distribution is obtained, parameters such as equivalent reflectivity factor, attenuation, terminal velocity, and rain rate can be calculated directly from the distribution. All four of these parameters are either measured or are products of the algorithm. The algorithm's results must be compared to the original data to ensure they are consistent. Divergent results would suggest that biases were not properly removed and the resulting $N(D)$s are not accurate.

The first parameter to compare is attenuation, which can be calculated with (6). Accurately determining the attenuation is crucial because the value obtained is used to correct the amplitude of the Doppler spectra and equivalent reflectivity factors and to determine the rain rate. Errors in the attenuation cause offsets in the drop concentrations between the frequencies as well. Reflectivity can be calculated from the drop size distribution with

$$Z_e = \frac{\lambda^4}{|K_w|^2 \pi^5} \int_0^\infty N(D)\sigma_b(D)\, dD, \tag{9}$$

where $\sigma_b(D)$ is the backscatter equation as a function of drop diameter. This can be compared to the attenuation-corrected reflectivity calculated by integrating the measured Doppler spectra over the velocity bins. The rain rate can be calculated with

$$R = \int_0^\infty N(D)D^3 v(D)\, dD, \tag{10}$$

where $v(D)$ is (4) with the air density correction factor. This can be compared with the rain-rate estimate resulting from the DWR comparison. Mean velocity can be calculated with

$$\overline{v} = \frac{\int_0^\infty N(D)\sigma_b(D)v(D)\,dD}{\int_0^\infty N(D)\sigma_b(D)\,dD}. \quad (11)$$

This can then be compared to the measured velocity with the vertical air motion removed.

TABLE 1. CPRS system parameters.

	Ka-band radar	W-band radar
Frequency	33.12 GHz	94.92 GHz
Peak power	100 kW	1.5 kW
Average power	120 W	15 W
PRF	200 Hz–1.5 kHz (20-kHz bursts)	1 Hz–80 kHz
Pulsewidth	200–1000 ns	50–2000 ns
Noise figure	11 dB	13 dB
3-dB bandwidth	2, 5 MHz	2, 5 MHz
3-dB beamwidth	0.5 deg	0.18 deg

3. Experiment and instrument

a. Ground-based remote sensing intensive observation period (GBRS IOP)

From 17 April to 7 May 1995, CPRS participated in the GBRS IOP, an experiment sponsored by the Department of Energy as part of the ARM program. The experiment took placed at the ARM's CART site in Lamont. During April squall-line systems develop to the southwest of the CART site and move either east or northeast, producing heavy rain and sometimes hail. Large formations of cirrus clouds typically precede the storms and continental stratus occur as well. This scenario provides a variety of cloud and precipitation cases to study.

During the experiment, radiosondes were launched every 3 h from a platform 130 m away from CPRS, and surface measurements of temperature and pressure were recorded every minute with a Surface Monitoring Observation System (SMOS) located 280 m away. Temperature and pressure profiles were extracted by adjusting the sonde data with the difference between the sonde's ground readings and the SMOS data at the time of observations.

b. Instrument

CPRS is a fully polarimetric Doppler radar consisting of two subsystems at 33 and 95 GHz (Sekelsky and McIntosh 1996; Lohmeier et al. 1997). Parameters for the radar system are shown in Table 1. Both radar subsystems transmit and receive vertical- and horizontal-polarized pulses through a single 1-m lens antenna (Mooradd 1993). The single antenna design ensures that both frequencies sample the same cloud volume. Note, the different antenna beamwidths have negligible effects when comparing data between frequencies for two reasons: 1) by averaging distributed targets in time, the sample volumes at the two frequencies are similar, and 2) the size of the sample volumes are accounted for in the radar's calibration constants (Sekelsky and McIntosh 1996). The transmit polarization can be selected on a pulse-to-pulse basis, and each subsystem has receiver channels that simultaneously record the amplitude and phase of copolarized and cross-polarized backscattered signals. The data acquisition system consists of six digitizers to record the log-magnitude power and limited I and Q for each receiver channel, as well as a DSP card to perform averaging and to compute either pulse pairs (Doppler moments) or FFTs (Doppler spectra) (Doviak and Zrnić 1993). CPRS is capable of measuring equivalent reflectivity factor (Z_e), linear depolarization ratio (LDR), mean Doppler velocity, velocity spectral width, as well as the full Doppler spectrum. The entire radar system is mounted on an azimuth-over-elevation positioner to perform RHI, PPI, VAD, and raster scans.

c. Doppler spectrum mode

When CPRS operates in the Doppler spectral mode, 64-point FFTs are performed for range gates from 200 m to as many as 20 range gates above the cloud tops. Extra range gates are taken so that the maximum number of range gates with no cloud or precipitation can be used to calculate a noise estimate to subtract from the data. Once the spectra are obtained, equivalent reflectivity factor, mean velocity, and velocity spectral width can be estimated with moment calculations (i.e., Z_e = 0th moment, v = 1st moment, σ_v = 2d moment).

The spatial and temporal variations of the vertical wind in rain requires that the millimeter-wave radars be sensitive enough to measure the backscatter and Doppler frequency shift from rain cells having dimensions of tens of meters. The transmitted powers and noise figures of CPRS provide adequate signal-to-noise ratios that allow drop size retrievals for 60-m range gates and requires 2 s of integration to achieve these signal-to-noise levels. Thus, if we assume the clouds move horizontally at a maximum of 30 m s^{-1}, the horizontal displacement of the precipitating clouds is less than 60 m during each sampling interval.

4. Observations and analysis

We present two cases of Doppler spectra for rain: a stratiform rain event occurring on 22 April 1995 and a transition region rain event occurring on 24 April 1995. Range and temporal resolution are 60 m and 2 s, re-

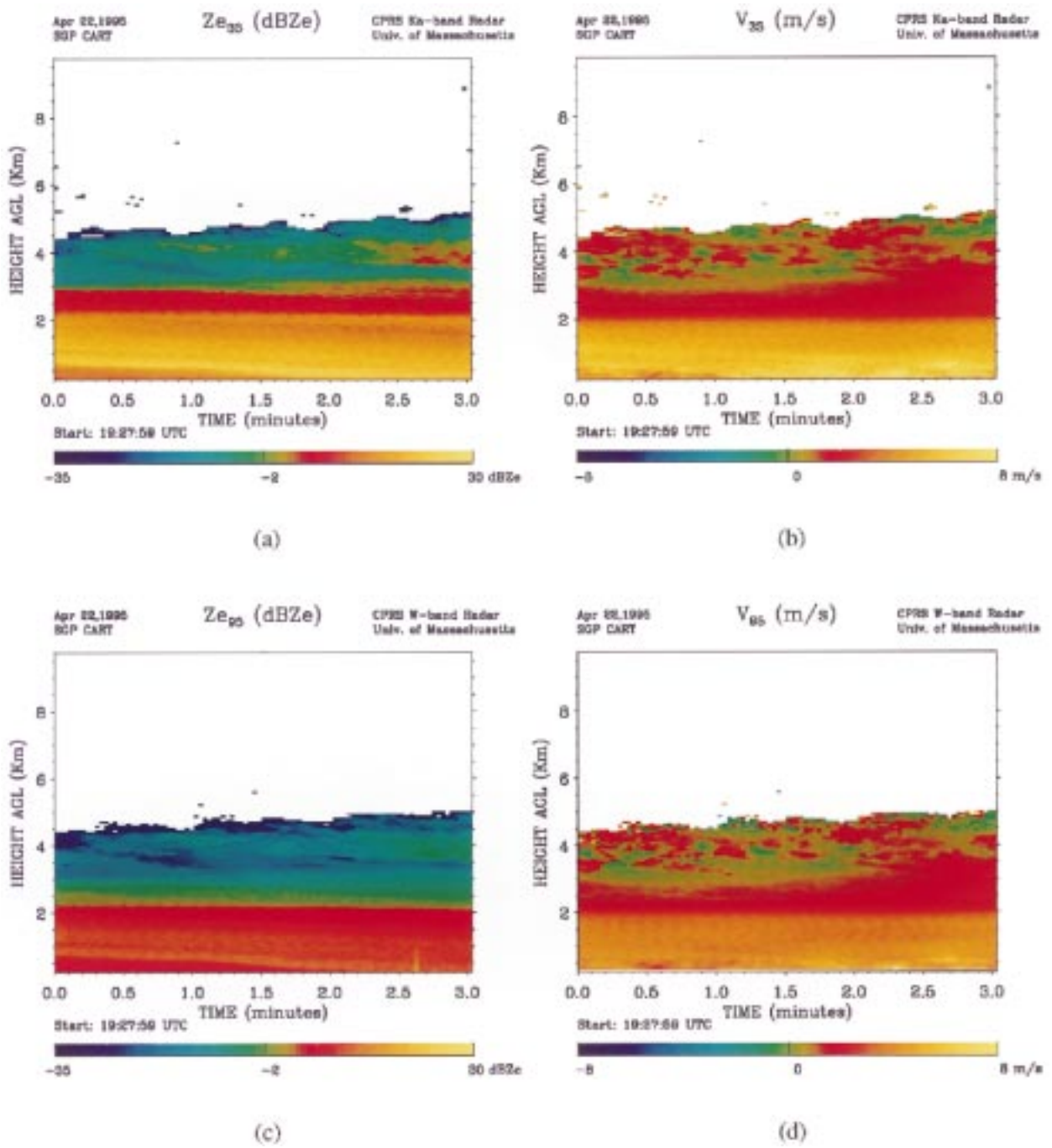

FIG. 6. CPRS images of equivalent reflectivity factor and velocity of a stratiform region of a rain storm UTC 1927:59 22 April 1995, (a) 33-GHz reflectivity, (b) 33-GHz mean fall velocity, (c) 95-GHz reflectivity, (d) 95-GHz mean fall velocity. The images have 2-s resolution and 60-m range gates.

spectively. The first case was used as a simple scenario to study, as the vertical wind field appeared to be weak and uniform. The second case presented a more complex situation for the algorithm to resolve because greater activity was evident in the ice clouds and the rain. Note, the data are presented with the sign of the vertical air motion opposite to the meteorological convention.

a. Case 1: Stratiform rain event on 1927:59 UTC 22 April 1995

Figure 6 shows images of equivalent reflectivity factor and velocity for 33 and 95 GHz, respectively. The Doppler spectra are taken 4 h after an anvil cloud. Over those 4 h, the cloud top descended from approximately

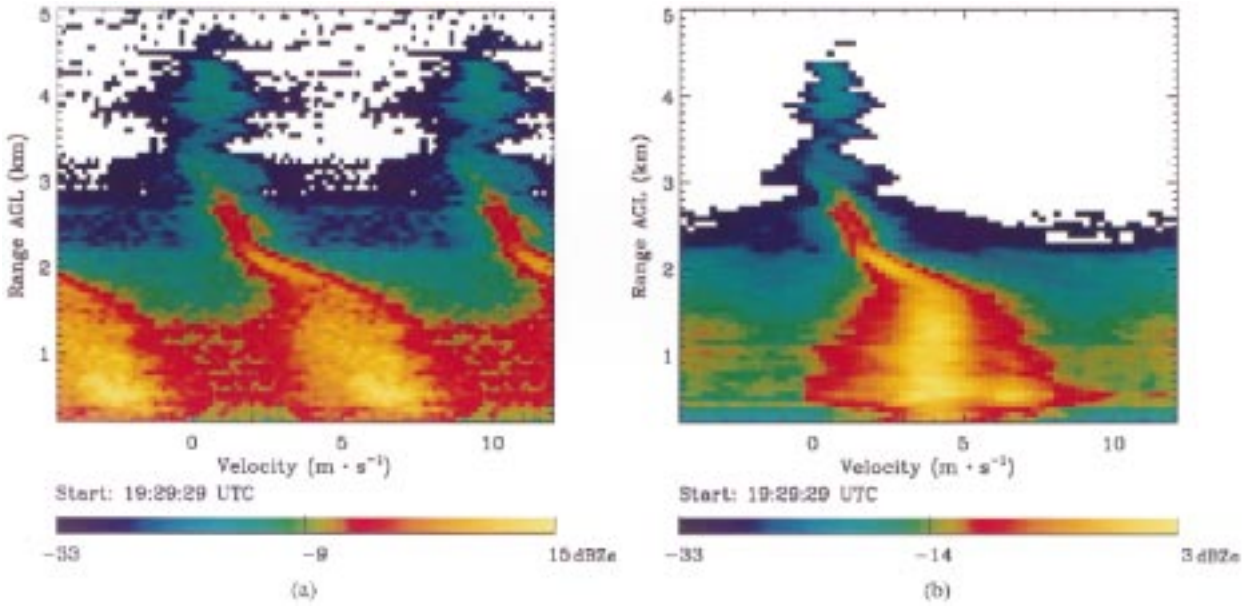

FIG. 7. Doppler spectra of rain at (a) 33 GHz and (b) 95 GHz for 1929:29 UTC 22 April 1995. Notice the increase in spectral width as the particles descend from the ice region through the melting layer into the rain.

10 to 5 km and stabilized. During the spectral measurements, the rain fell lightly. Figure 7 shows an example of the spectral measurements. The evolution of particle phase can clearly be identified by the abrupt changes in velocity and spectral width as ice falls through the melting layer and converts to liquid water. The sharp increase in velocity from 1.8 to 2.3 km in range indicates that presence of a melting layer. Measurements of LDR close in time to this file and the detection of a 0°C isotherm from a radiosonde confirm the location of the melting layer. Animation of the spectral images showed only small variations in the mean velocity and spectral width over time. Note, the double image in the 33-GHz Doppler spectrum is due to velocity foldover caused by pulse repetition frequency (PRF) limitations of the 33-GHz transmitter while operating in the Doppler spectral mode. The 95-GHz Doppler spectrum does not exhibit this effect because the transmitter can be run at an adequate PRF.

Our DF algorithm was applied to spectra for range bins of 60 m for altitudes from 0.2 to 1.6 km. Two seconds of data were used to obtain the spectra. The $N_{33}(D)$ and $N_{95}(D)$ were highly correlated in the drop diameter region from 0.5 to 3 mm, but diverged at larger drop sizes and in some cases diverged for diameters from 0.5 to 0.65 mm, as shown in Fig. 8a. Error bars for $N_{33}(D)$ and $N_{95}(D)$ are also shown, which were generated by retrieving distributions while adding and subtracting one 95-GHz Doppler bin, 0.247 m s^{-1}, to the vertical air motion estimate and calculating the difference between the distributions with and without the induced error. Note, the units on the error graphs are the same as the $N(D)$ graph, just with a smaller scale. One would expect to see the 95-GHz signal detect the smaller drops better than 33 GHz, however, because of its increased sensitivity to small particles due to the λ^{-4} dependence in the backscattering equation. Although the overall sensitivity of the 33-GHz subsystem is about 2 dB higher than the 95-GHz subsystem for any sized drop (Sekelsky and McIntosh 1996), the 95-GHz subsystem collects approximately 10 times the number of spectra per second in the Doppler spectral mode, providing 5 dB more sensitivity. Thus, the 33-GHz spectral point for small drops had an insufficient signal-to-noise ratio to determine a drop concentration. Note, for example, that the noise floor estimates track along with drop size estimate from 3 to 5 mm for both frequencies and from 0.5 to 0.65 mm for 33 GHz. The divergence does not imply that the results are suspect or of limited use, however. Considering that the rain rates associated with these seemingly narrow drop estimates are relatively low, the population of large drops may be very small. Moreover, in millimeter-wave calculations involving the drop size distribution, the statistically significant contribution comes from the drop diameter range of 0.5–3.0 mm (Lhermitte 1990). For example, the $N(D)$s for 1929:29 UTC were used to calculate equivalent reflectivity factor and velocity in range and then compared to measured quantities as shown in Figs. 8b and 8c, respectively. Equations (9) and (11) were applied to the retrieved $N(D)$s to calculate equivalent reflectivity factor and velocity, integrating from 0.5 to 3.0 mm. The measured equivalent reflectivity factors were corrected with attenuation calculated with (6), and the measured mean velocities were corrected with the vertical air motion determined from the retrieval algo-

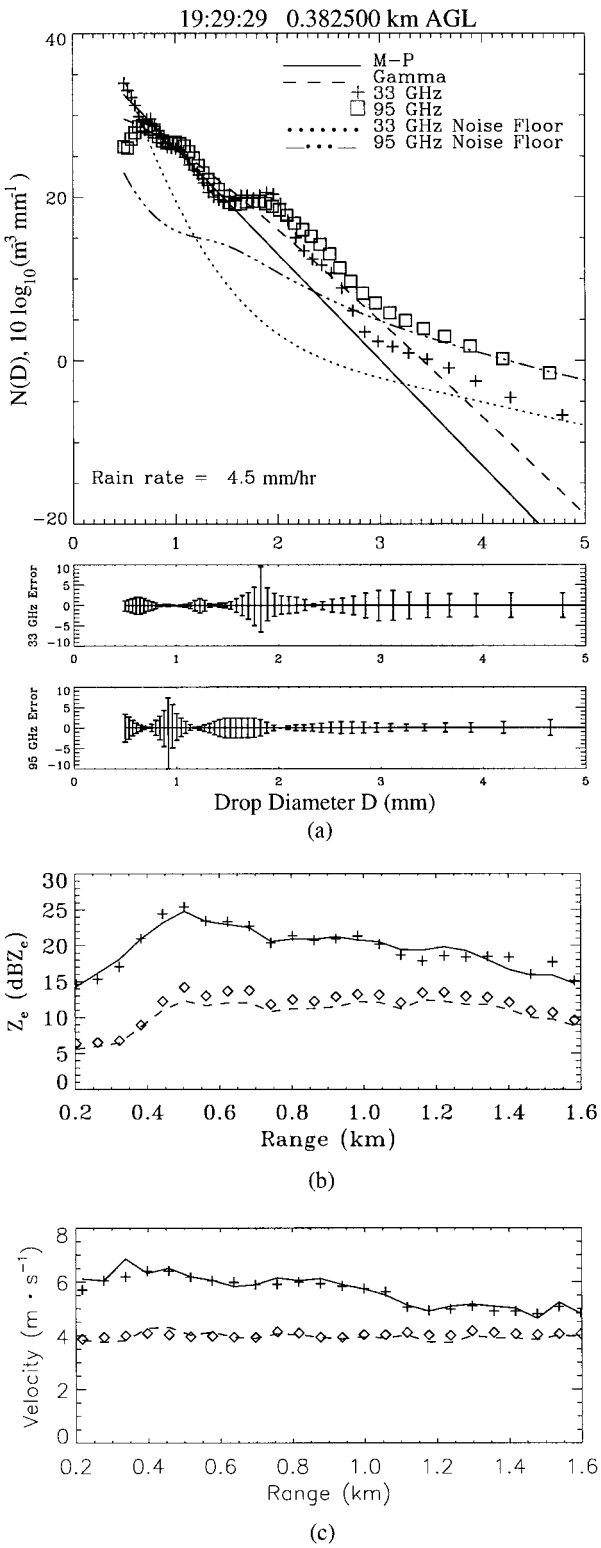

FIG. 8. (a) Retrieved $N_{33}(D$ and $N_{95}(D)$ along with Marshall–Palmer and gamma distributions for 1929:29 UTC 22 April 1995. Notice the high degree of correlation from 0.65 to 3.0 mm. Also notice the retrieved distributions do not strictly follow either model. (b) Comparison of attenuation-corrected equivalent reflectivity factor (33 GHz = solid line, 95 GHz = dashed line) and $N(D)$-calculated equivalent reflectivity factor (33 GHz = +, 95 GHz = ◇), where $\sigma_{Z_{33}}$ = 0.72 dB, and $\sigma_{Z_{95}}$ = 0.54 dB. (c) Mean velocity with vertical air motion correction (33 GHz = solid line, 95 GHz = dashed line) compared to mean velocity calculated from $N(D)$ (33 GHz = +, 95 GHz = ◇), where $\sigma_{v_{33}}$ = 0.13 m s^{-1}, and $\sigma_{v_{95}}$ = 0.12 m s^{-1}. Notice the retrieval results are consistent with the radar measurements.

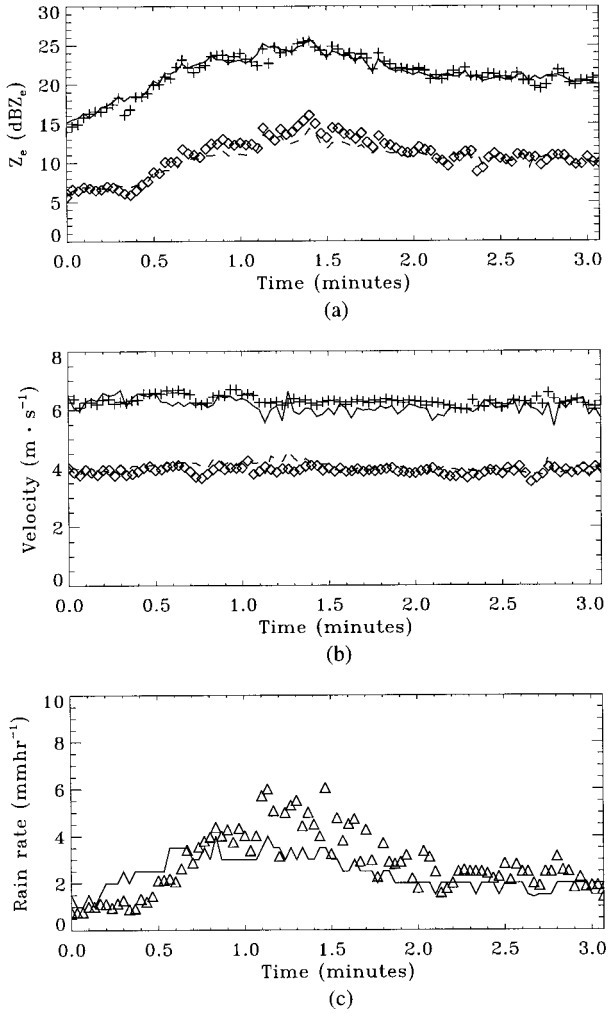

FIG. 9. Plots of self-consistency in time for stratiform rain at the 0.5625-km range gate. Measured quantities in (a) and (b) are represented by 33 GHz = solid line, 95 GHz = dashed line, and quantities calculated with retrieved $N(D)$s are represented by 33 GHz = +, 95 GHz = ◇. (a) Attenuation-corrected equivalent reflectivity factor compared to integrated equivalent reflectivity factor, $\sigma_{Z_{33}}$ = 0.80 dB and $\sigma_{Z_{95}}$ = 0.63 dB. (b) Vertical air motion corrected mean velocity compared to integrated mean velocity, $\sigma_{v_{33}}$ = 0.24 m s^{-1} and $\sigma_{v_{95}}$ = 0.16 m s^{-1}. (c) DWR-derived rain rate (solid line) compared to $N(D)$-integrated rain rate, σ_{Rr} = 0.94 mm h^{-1}.

rithm. The measurements and calculations compare well for both quantities at both frequencies. The standard deviations between equivalent reflectivity factors were 0.72 and 0.54 dB, and for mean velocities were 0.13

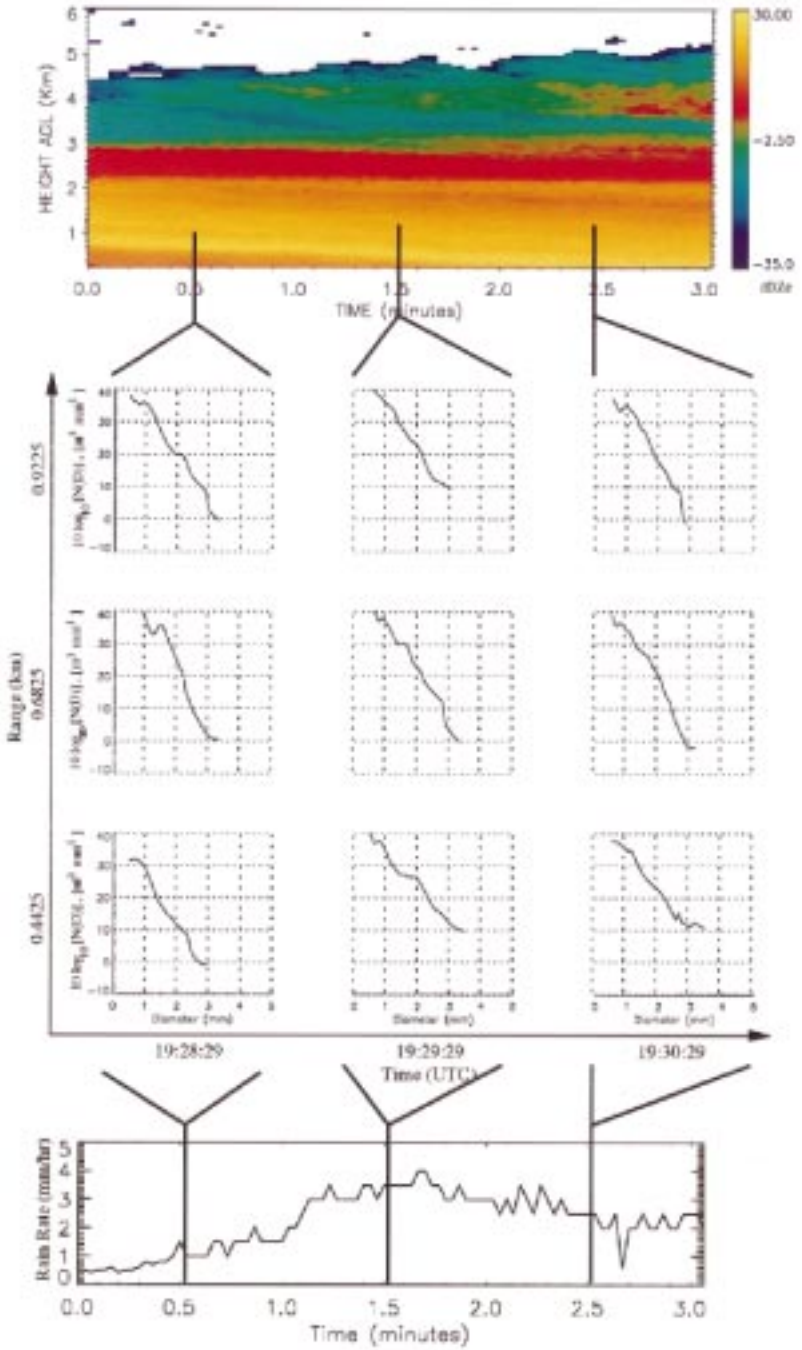

FIG. 10. Waterfall plot of retrieved $N(D)$s for 22 April 1995. (Top) The 33-GHz reflectivity. (Bottom) The rain rate at 0.4425 km.

and 0.12 m s^{-1} for 33 and 95 GHz, respectively. Figure 9 shows that comparisons between measured and calculated quantities demonstrate similar agreement in time. A single range gate at 0.5625 km for all the time profiles was analyzed similarly for equivalent reflectivity factor and velocity, and (10) was used to estimate rain rate. The standard deviations between equivalent reflectivity factors were 0.80 and 0.63 dB, and for mean velocities they were 0.24 and 0.16 m s^{-1} for 33 and 95 GHz, respectively. The standard deviation for rain rate is 0.94 mm h^{-1}. Notice also the rain-rate estimate tracks along with the equivalent reflectivity factor, increasing until about 1.4 min and then decreasing.

Figure 10 shows a waterfall plot of several retrieved

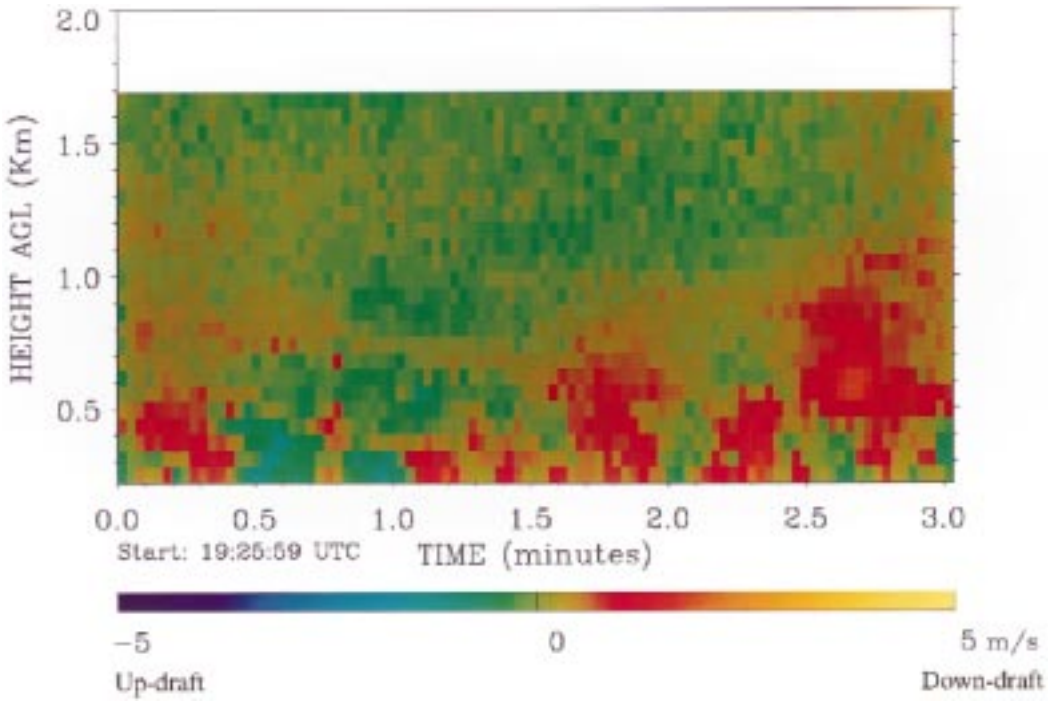

FIG. 11. Estimated vertical air motion initializing the algorithm with a Marshall–Palmer drop size distribution. The vertical wind is close to 0 m s^{-1} for most range gates. Small updrafts and downdrafts (≈1 m s^{-1}) occur in the bottom 500 m.

$N(D)$s along with a 33-GHz equivalent reflectivity factor image and a rain-rate estimate. The bold vertical lines indicate the times that these samples were taken. The rain-rate estimate is taken from the 0.4425-km range gates. Higher drop concentrations and flatter slopes are observed for the higher rain rates. The band of low equivalent reflectivity factor at the low range gates in the beginning of the file are seen in the distributions for 1928:29 UTC as well. The 0.4425-km range gate has lower drop concentrations than the range gates above.

Figure 11 shows the vertical wind for this case. For the most part, the winds are at or near zero, as one would expect for precipitation from stratiform clouds. In the bottom 500 m we see small updrafts and downdrafts with values on the order on 1 m s^{-1}. Small deviations from the mean velocity were observed while animating the spectra consistent with the vertical air motion estimates. Figures 6b and 6d compare well to the location of updrafts and downdrafts in Fig. 11, and the mean fall velocities corrected with the vertical air motion estimates in Figs. 8c and 9b show similar agreement as well.

The rain-rate estimate used to initialize the algorithm can be compared to a rain gauge on a larger timescale by comparing total precipitation. Doppler spectra were only collected a few minutes at a time, and pulse-pair measurements were taken in between. Longer time series are required for a rain-gauge comparison. However, the pulse-pair measurement provide the same sample pair of equivalent reflectivity factors at 33 and 95 GHz needed to estimate DWR, so (7) can be used to estimate rain rate over a larger timescale to compare to the rain gauge. Using the DWR curve in Fig. 4c and the attenuation curve in Fig. 4b, rain rates were estimated from 1800 to 2030 UTC, which corresponds to approximately 1.5 h before to 1 h after the Doppler spectral measurements. A single frequency rain-rate estimate was generated using 33-GHz equivalent reflectivity factor and Figs. 4a,b as well. The rain rates were then integrated over time for a total precipitation estimate. The rain gauge, located on the SMOS, provided total precipitation estimate in 0.254-mm increments. Total precipitation was calculated by adding the bucket count over time. Figure 12 shows the total precipitation estimates from the SMOS rain gauge, DWR, and $Z_{e_{33}}$ estimates. The rain gauge and dual-frequency (DWR) estimates show excellent agreement from 1800 to 1900 UTC. Discrepancies after this can be accounted for by two factors. First, surface winds can knock over the rain bucket, causing it to empty prematurely. Second, the rain gauge is located 280 m from the radar, and the storm motion was nearly perpendicular to a line connecting the two. In contrast to the DWR estimate, the single-frequency (33-GHz equivalent reflectivity factor) estimate is consistently lower than the rain-gauge estimate. This may be due to a greater dependence on the drop size distribution model used to derive the relationships in Fig. 5 by virtue of the ratio in the DWR calculation, which

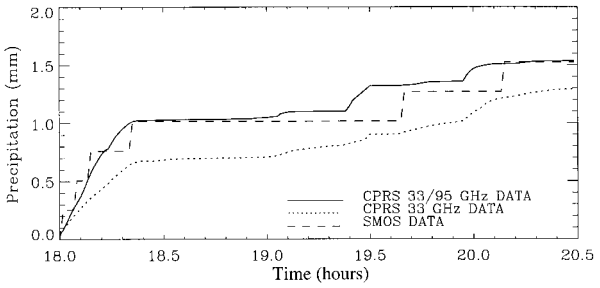

FIG. 12. Comparison of total precipitation estimates derived from CPRS DWR, 33-GHz equivalent reflectivity factor, and rain-gauge data from the SGP CART site for 1800–2030 UTC 22 April 1995. Notice the dual-frequency estimate is closer to the rain-gauge data than the single-frequency estimate.

diminishes the dependence on the magnitude offsets in the model.

b. Case 2: Transition region rain event on 2059:29 UTC 24 April 1995

The second case studied was in the region of a storm about 50 min after the leading edge of an anvil cloud. The storm had not progressed into the stratiform rain state observed in case 1, but instead the convection was decaying. In this case, several variations in the wind and rain rate were noted in the log book, thus this case poses a more difficult scenario. Equivalent reflectivity factor and velocity images plotted in Fig. 13 indicate the presence of a melting layer located from 1.0 to 1.5 km AGL and above that large formations of swirling ice and snow, sometimes causing regions of increased precipitation. This is clearly evident from 1.5 to 2.0 min, where the equivalent reflectivity factor becomes higher in the rain while lower in the clouds, indicating an increase in extinction. One can infer the particle phase by examining a time profile of the spectra such as shown in Fig. 14. As the particles fall from the top of the cloud to the melting layer, the reflectivities gradually increase and mean velocities vary around a value of 1 m s^{-1} for both frequencies. The onset of melting is identified by the sharp increase in equivalent reflectivity factor and velocity progressing to raindrops as the spectral width broadens. Animation of the spectra revealed that the mean velocity varied significantly over time and in range, implying the presence of multiple updrafts and downdrafts. For example, the mean velocity in Fig. 14 varies by as much as 2 m s^{-1}, while the equivalent reflectivity factor is relatively flat. Changes in the rain rate cannot account for these large velocity variations.

Our DF algorithm was applied to spectra for the range gates from 0.2 to 1.0 km AGL in 60-m range increments and from 2059:29 to 2106:25 UTC in 2-s time averages for both frequencies. In most cases, the $N_{33}(D)$ and $N_{95}(D)$ were highly correlated. Figure 15a shows retrieved distributions for 2100:25 UTC along with noise estimates, an M–P distribution, and a gamma distribution ($\mu = 1$). Error bars were generated in the same way as the stratiform case. The two frequencies show excellent agreement in shape and magnitude. However, they do not strictly follow the shape of either of the models. For instance, the distributions match M–P for the small drop region (0.5 to 0.9 mm), but they match the gamma distribution for the larger drops (1.5 to 4 mm). The dip at 1.4 mm is interesting as well. At first this may seem to be an artifact of the algorithm caused by an inappropriate turbulence calculation, such as demonstrated in Fig. 5. However, only one dip occurs over the distributions and at the same location for both frequencies. If the effect were an artifact, several dips and peaks should appear in $N_{95}(D)$, and only one should occur in $N_{33}(D)$ at about 4.25 mm.

The $N(D)$s for 2100:25 UTC were used to calculate equivalent reflectivity factor and fall velocity using (9) and (11), respectively, and then compared to the measured quantities as shown in Figs. 15b,c. The measured equivalent reflectivity factors were corrected with attenuation calculated with (6), and the velocities were corrected by subtracting the vertical air motion estimate from the measured mean velocities. The standard deviations between equivalent reflectivity factors were 0.65 and 0.60 dB and for mean velocities were 0.31 and 0.28 m s^{-1} for 33 and 95 GHz, respectively. The high degree of correlation between the measurements and calculations at both frequencies implies that the results are self-consistent. Figure 16 shows a similar comparison, where (9), (11), and (10) were used to compare (a) equivalent reflectivity factor, (b) velocity, and (c) rain rate over time for the 0.4425-km range gate. The standard deviations between equivalent reflectivity factors were 2.3 and 1.1 dB and for mean velocities were 0.55 and 0.27 m s^{-1} for 33 and 95 GHz, respectively. The equivalent reflectivity factors and velocities at both frequencies agree reasonably well except in the time from 4.3 to 5.3 min. The error is due to the low rain rate in this time interval, making it difficult to distinguish the Mie null and casting suspicion on the vertical air motion estimate. Consider Fig. 16c, which compares rain rates, with a standard deviation of 2.5 mm h^{-1}. The rain rate dips below 1 mm h^{-1}, and the equivalent reflectivity factor and velocity comparisons do not compare well. Thus, below a minimum rain-rate threshold of about 1 mm h^{-1}, which corresponds to a peak signal-to-noise ratio of 15.5 dB in the 95-GHz Doppler spectra, the retrievals suffer large errors. This number can vary, however, depending on turbulence: with higher turbulence, higher rain rates are required to distinguish the Mie null. Figure 17 shows a waterfall plot of several retrieved drop size distributions. The slope of the distributions are clearly evident at different rain rates. For example, the distributions at 2101:29 UTC occur during increased precipitation, and they have a higher concentration of large drops. The rain rate is much higher at this time as well. The steep distributions at 2104:29

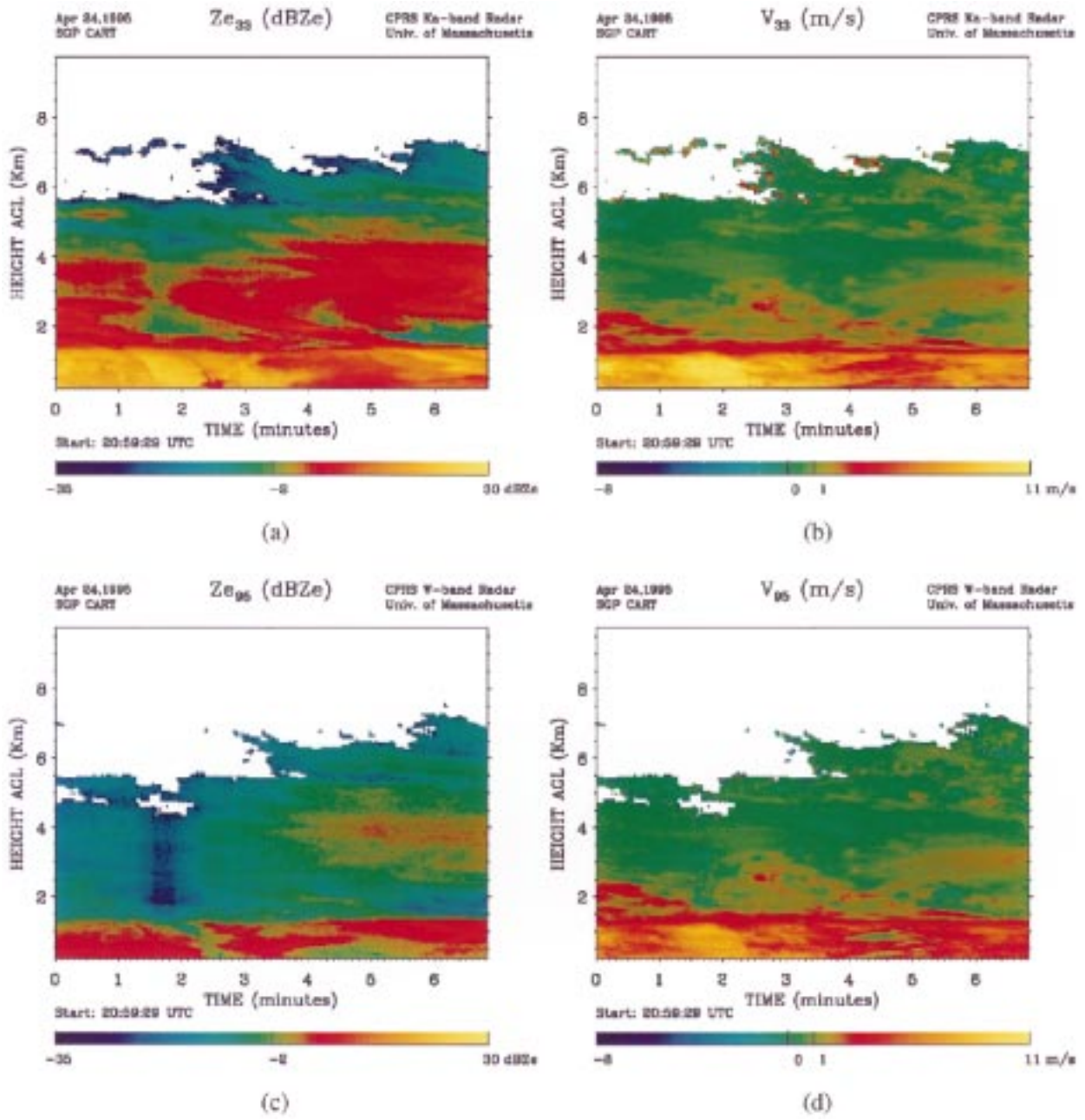

FIG. 13. CPRS images of equivalent reflectivity factor and velocity of a rain storm on 2059:29 UTC 24 April 1995. (a) 33-GHz equivalent reflectivity factor, (b) 33-GHz mean fall velocity, (c) 95-GHz equivalent reflectivity factor, and (d) 95-GHz mean fall velocity. The images have 2-s averages and 60-m range gates. A region of increased precipitation is seen from 1.5 to 2.0 min in the file as the equivalent reflectivity factors increase in the rain and decrease in the ice clouds. Also notice the variations in velocity fromn 0.2 to 1.0 km AGL.

are in a region of light rain and drizzle, where the estimated rain rate has fallen to approximately 1 mm h^{-1}. Notice also that the drop concentration estimates are consistent in range for all three time profiles.

Figure 18a shows an image of the estimated vertical air motion, and Fig. 18b shows sample profiles of vertical air motion where five profiles (10 s) were grouped every 60 s, starting from 2059:29 UTC. The velocity scale on each set of profiles is ± 5 m s^{-1}, except for the first set, which only extend from 0–5 m s^{-1}. The profiles at the beginning of the file show a consistent downdraft with decreasing intensity from the melting layer to the ground. This is expected as the vertical velocity must be zero at the ground. Just after this, the wind pattern resembles a saw tooth, with a downdraft from 0.2 to 0.4 km and then again at 0.7 to 1.0 km with an updraft

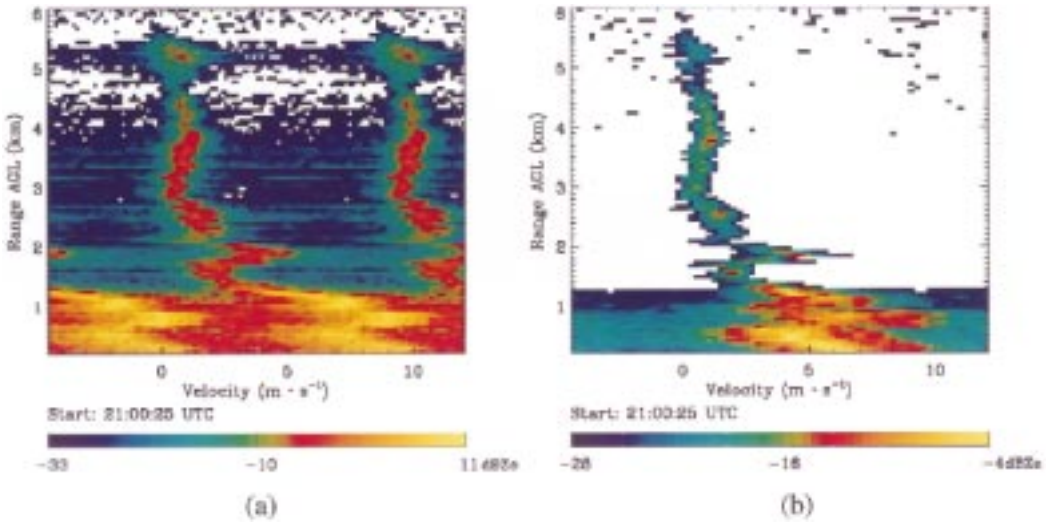

FIG. 14. Doppler spectra of rain at (a) 33 GHz and (b) 95 GHz for 2100:25 UTC 24 April 1995. Large variations in mean velocities are observed, while the reflectivities are relatively smooth.

in the middle. This progresses to a stronger (higher velocity) uniform downdraft, which occurs during the heavier rain. The sawtooth pattern returns after the cell of intense precipitation passes, but 7 min after this, the orientation of opposing updrafts and downdrafts switches as an updraft occurs close to the ground and near the top of the precipitation. This progresses to a uniform updraft and then a downdraft that reverts back to the sawtooth at the end of the file, which now varies about 0 m s^{-1}. Figures 13b and 13d compare well to the location of updrafts and downdrafts in Fig. 18, and the mean fall velocities corrected with the vertical air motion estimates in Figs. 15c and 16b show similar agreement as well.

5. Conclusions

A primary source of error in the algorithm is from the vertical air motion estimate, which is determined by correlating measured and modeled Doppler spectra based on the Mie null location. This error can be as large as the dimension of the 95-GHz Doppler velocity bins, 0.247 m s^{-1}, which was demonstrated in the error bars presented in Figs. 8a and 15a. The effect that the drop size distribution model used to initialize the algorithm has on our results is also of interest. The iterative steps that use retrieved drop size distributions in place of the initial model should lead to a closer approximation to the measured Doppler spectra and a better estimate of the vertical air motion. To determine if this is true, the estimated vertical air motion was compared after initializing the algorithm with different models and iterating with retrieved distributions. This effect was also analyzed by simulating Doppler spectra while adding vertical air motion and varying amounts of turbulence. Vertical air motion was then extracted from these simulations and compared to the actual value. The resulting drop size distributions were also analyzed for both the experimental and simulated Doppler spectra to determine how vertical air motion differences affect drop concentration estimates.

a. Vertical air motion estimates

The vertical air motion estimates were relatively independent of the model distribution used to initialize the algorithm. Results using an exponential model were compared to those using gamma models with $\mu = 1$ and -1 after iterating the correlation five times. The vertical air motion estimates presented in Figs. 11 and 18 were obtained initializing with an exponential model. After rerunning the algorithm using the gamma models, the shape of the vertical air motion profiles agreed well when all three drop size distributions were used to initialize the algorithm for both the stratiform and transition region rain cases. By using retrieved drop size distributions for adjacent pixels, any bias from the initial model is removed and the difference between vertical air motion estimates is negligible, as in most cases the mean and standard deviation of the differences between the vertical air motion estimates converged to zero. When the vertical air motion did not converge, the differences were less than 0.1 m s^{-1}. It was also discovered that the $\mu = -1$ gamma model gave a higher estimate and the $\mu = 1$ gamma model gave a lower estimate of vertical air motion than when using an exponential model.

Doppler spectra were simulated with an exponential model and altered with velocity shifts and turbulence. The analysis covered turbulence widths varying from 0.0–2.0 m s^{-1} and rain rates from 0.1 to 20 mm h^{-1}. Then the three drop size distribution models previously

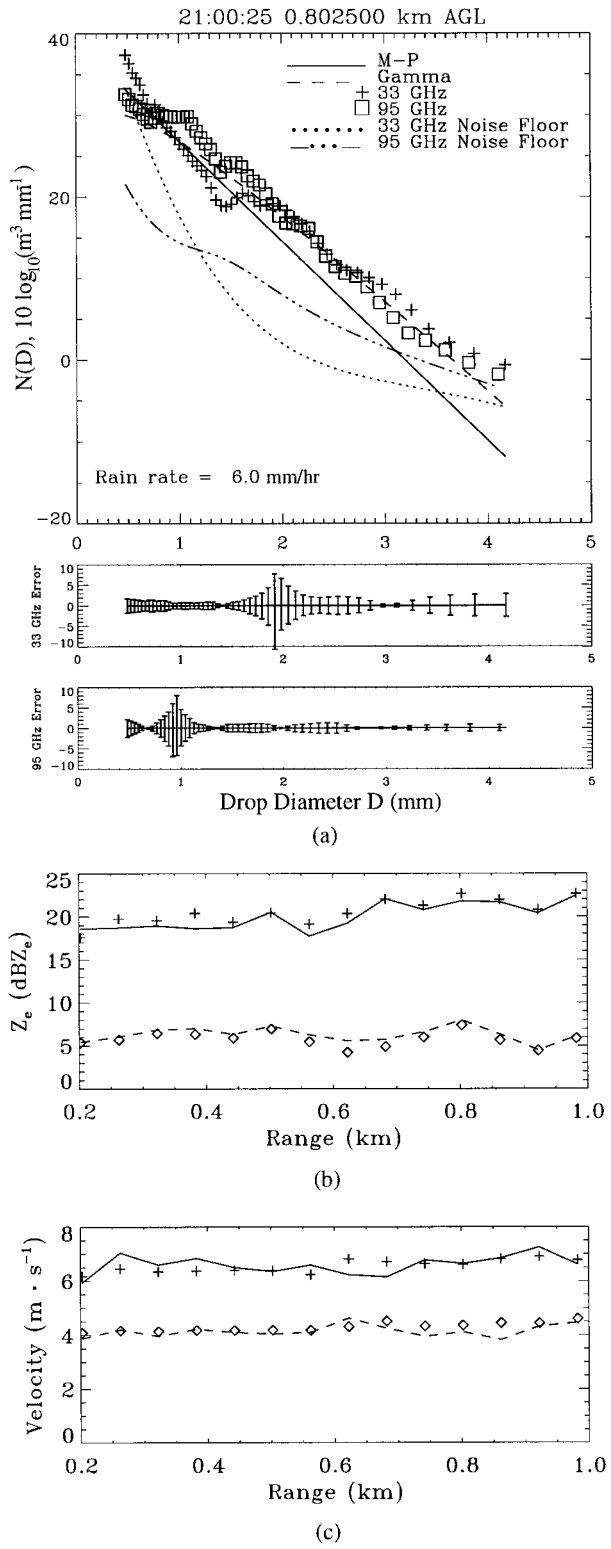

FIG. 15. (a) Retrieved $N_{33}(D)$ and $N_{95}(D)$ along with Marshall–Palmer and gamma distributions for 2100:25 UTC 24 April 1995. Notice the two distributions are highly correlated over the range of drop diameters but do not strictly follow the shape of the models (e.g., the dip at 1.4 mm). (b) Attenuation-corrected equivalent reflectivity factor (33 GHz = solid line, 95 GHz = dashed line) compared to equivalent reflectivity factor calculated with retrieved $N(D)$s (33 GHz = +, 95 GHz = ◇), where $\sigma_{Z_{33}}$ = 0.65 dB and $\sigma_{Z_{95}}$ = 0.60 dB. (c) Mean velocity with vertical air motion correction (33 GHz = solid line, 95 GHz = dashed line) compared to mean velocity calculated from retrieved $N(D)$s (33 GHz = +, 95 GHz = ◇), where $\sigma_{v_{33}}$ = 0.31 m s^{-1} and $\sigma_{v_{95}}$ = 0.28 m s^{-1}.

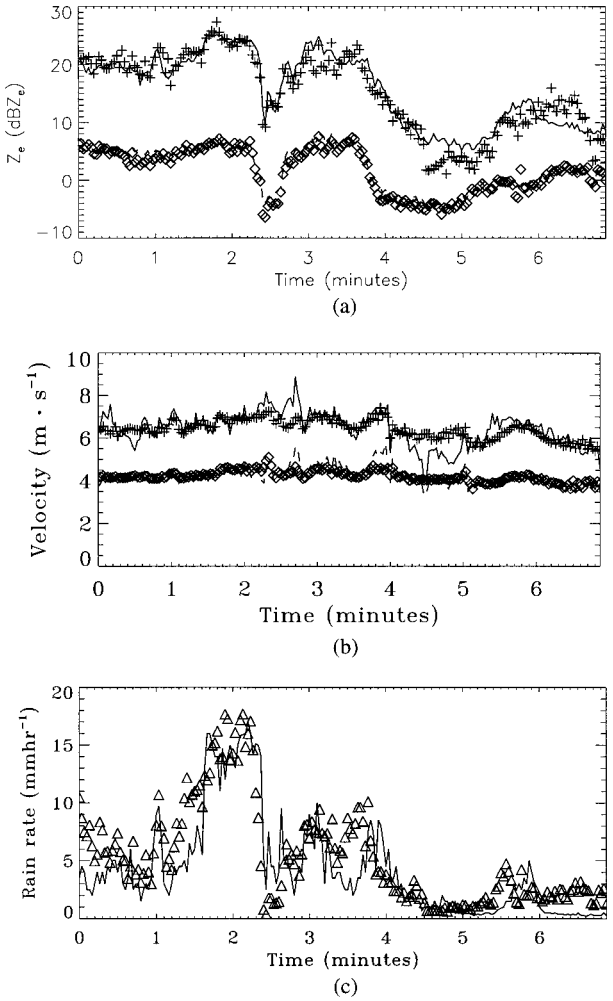

FIG. 16. Self-consistency in time for transition region rain at the 0.4425-km range gate. In (a) and (b), measured quantities are represented by 33 GHz = solid line, 95 GHz = dashed line, and quantities calculated with retrieved $N(D)$s are represented by 33 GHz = +, 95 GHz = ◇. (a) Attenuation-corrected equivalent reflectivity factor compared to integrated equivalent reflectivity factor, where $\sigma_{Z_{33}}$ = 2.3 dB and $\sigma_{Z_{95}}$ = 1.1 dB. (b) Vertical air motion–corrected mean velocity compared to integrated mean velocity, where $\sigma_{v_{33}}$ = 0.55 m s^{-1} and $\sigma_{v_{95}}$ = 0.27 m s^{-1}. (c) DWR-derived rain rate (solid line) compared to $N(D)$-integrated rain rate, σ_{Rr} = 2.5 mm h^{-1}. These plots show self-consistency except when the rain rate falls below approximately 1.0 mm h^{-1}.

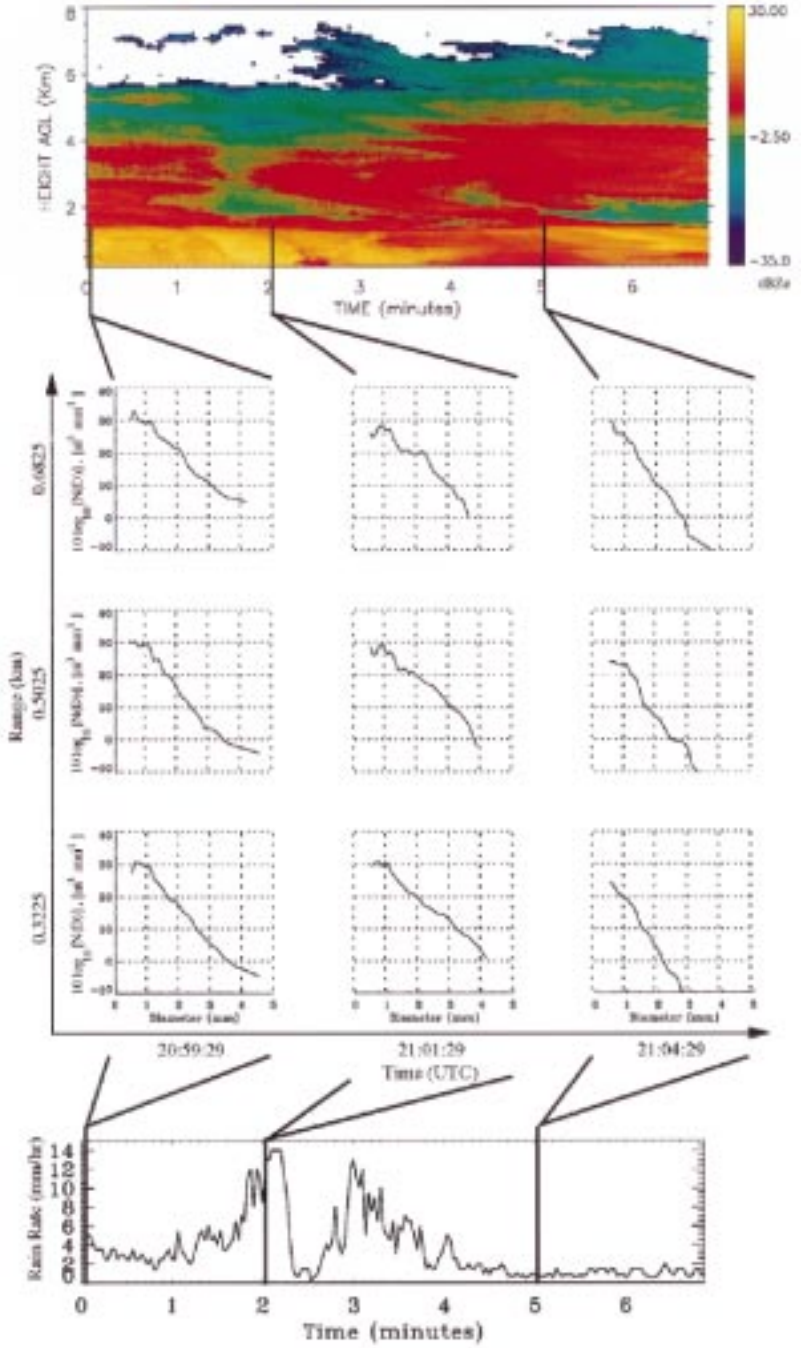

FIG. 17. Waterfall plot of retrieved $N(D)$s for 24 April 1995. (Top) The 33-GHz reflectivity and (bottom) rain rate.

discussed were used to initialize the retrieval algorithm, and the vertical air motion estimate was compared to the induced velocity shift. When the algorithm was initialized with the exponential model, the vertical air motion estimate had no errors on the first iteration for rain rates greater than 1 mm h^{-1} when turbulence was less than 1.5 m s^{-1}. Below 1 mm h^{-1}, the vertical air motion estimate diverged after iterating the correlation. Similar results were obtained from retrievals initialized with gamma models. For rain rates higher than 1 mm h^{-1}, the vertical air motion converged after two or three iterations when turbulence was less than 1.5 m s^{-1}. At rain rates lower than 1 mm h^{-1}, the $\mu = -1$ vertical air motion error diverged with additional iterations,

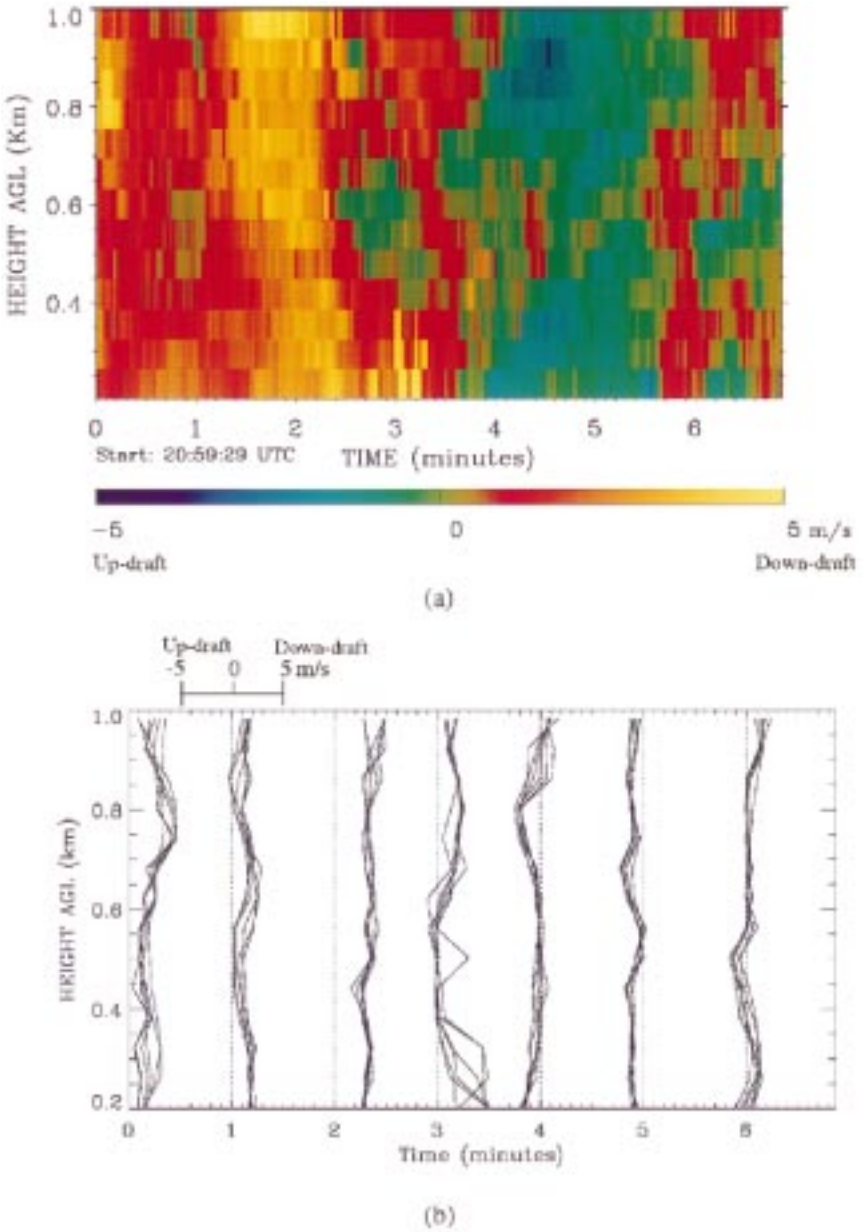

FIG. 18. (a) Estimated vertical air motion initializing the algorithm with a Marshall–Palmer drop size distribution. (b) Profiles of vertical air motion plotted every 60 s. The first 10 s (5 profiles) are plotted about the dotted lines (0 m s^{-1} reference lines for each 60-s interval), starting at 2059:29 UTC. The velocity scale in the upper-left-hand corner applies to each dotted line. The progression of the updrafts and downdrafts can be identified by examining the image and profiles.

while the $\mu = 1$ case decreased to 0.07 m s^{-1} but did not converge to zero.

b. Drop concentration estimates

The drop size distributions retrieved using different initial models showed small variations in concentration as well. The differences in drop concentrations were analyzed by calculating the normalized-integrated difference with

$$\overline{N}\overline{I}\overline{D}_{i,j} = \frac{\int |N_i(D) - N_j(D)|\, dD}{\int (N_i(D)N_j(D))^{1/2}\, dD}, \qquad (12)$$

where $N_i(D)$ and $N_j(D)$ are the drop size distributions retrieved initializing the algorithm with an exponential model, a gamma ($\mu = 1$) model, or a gamma ($\mu = -1$) model, and i and j refer to the constant μ. The nor-

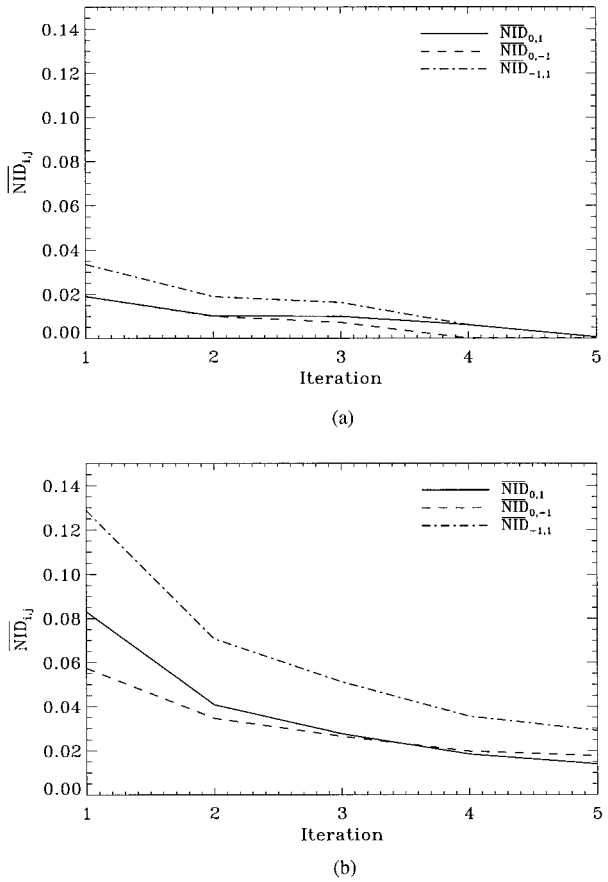

FIG. 19. Normalized-integrated difference between retrieved $N(D)$s initializing the algorithm with exponential and gamma models for (a) 22 April 1995 and 24 April 1995.

malized integrated differences were then averaged over time and range. Figure 19 shows the normalized-integrated difference between drop size distributions for the drop range between 0.5 and 3.0 mm for both sets of experimental data presented in the previous section. After iterating the algorithm, the difference between retrieved drop size distributions decreased, in some cases to zero.

The simulated Doppler spectra were put through the retrieval algorithm initialized with the three models, and the results were compared to drop size models used to generate the Doppler spectra. Error increased with rain rate because the total drop concentrations increased. It also increased the turbulence due to errors deconvolving the spectra.

c. Discussion

For stratiform and transistion region rain events, our algorithm was able to resolve the drop size distributions and vertical air motion with high temporal and range resolution. The drop concentration estimates for both frequencies agreed well in shape and magnitude for the most statistically significant portion of the drop diameter range. A rain-rate comparison showed that the dual-frequency estimate compared well with the CART site's rain gauge and outperformed a single-frequency estimate. Calculation of several parameters using the retrieved distributions showed excellent agreement with initial radar measurements as well, except in cases where the rain rate dropped below 1.0 mm h^{-1}, which corresponds to a peak signal-to-noise ratio of approximately 15.5 dB in the 95-GHz Doppler spectra. The signal must be high enough to distinguished the Mie effect in the presence of noise and turbulence. As expected, our results show that retrieved distributions do not strictly follow either an exponential or gamma model over the entire range of drops. Therefore, dual-frequency millimeter-wave radars have significant potential for improving estimates of drop size distribution.

For both the stratiform and transistion region rain, the shape of the vertical air motion profiles were highly correlated to each other, regardless as to which model was used to initialize the algorithm. The vertical air motion estimate is relatively insensitive to the initial model given that the rain rate is high enough to distinguish the Mie null in the presence of turbulence. Retrieved drop size distributions were also relatively independent of the initializing models except when the drop size was small. However, to reduce the number of iterations, the initial drop size model should be as close to the actual drop size distribution as possible.

Acknowledgments. This work was supported under by Department of Energy Atmospheric Radiation Measurement program (DOE Grant DE-FG02-90ER61060). The authors would like to thank the staff at the SGP CART site for their assistance during the GBRS IOP and also the staff at the ARM Data Archive for supplying us with data from site instruments. We would also like to acknowledge the efforts of several others who contributed to this research, including Greg Sadowy, Tim Scheve, and Mike Petrinino for their tireless efforts developing the data acquisition system; Lihua Li and Ray Bambha for helping to collect and process the data; and John Galloway and Andrew Pazmany assistance in analyzing the Doppler spectra and for discussions on millimeter-wave observations.

REFERENCES

Atlas, D., R. C. Srivastava, and R. S. Sekhon, 1973: Doppler radar characteristics of precipitation at vertical incidence. *Rev. Geophys. Space Phys.,* **11,** 1–35.

Battan, L. J., and J. B. Theiss, 1966: Observations of vertical motions and particle sizes in a thunderstorm. *J. Atmos. Sci.,* **23,** 78–87.

Caton, P. G. F., 1966: Raindrop size distributions in the free atmosphere. *Quart. J. Roy. Meteor. Soc.,* **92,** 15–30.

Doviak, R. J., and D. S. Zrnić, 1993: *Doppler Radar and Weather Observations.* 2d ed. Academic Press, 562 pp.

Foote, G. B., and P. S. duToit, 1969: Terminal velocity of raindrops aloft. *J. Appl. Meteor.,* **8,** 249–253.

Gossard, E. E., 1988: Measuring drop size distributions in clouds

with a clear-air-sensing Doppler radar. *J. Atmos. Oceanic Technol.,* **5,** 640–649.
——, R. G. Strauch, and R. R. Rogers, 1990: Evolution of drop size distributions in liquid precipitation observed by ground-based Doppler radar. *J. Atmos. Oceanic Technol.,* **7,** 815–828.
Green, A. W., 1975: An approximation for the shape of large raindrops. *J. Appl. Meteor.,* **14,** 1578–1583.
Gunn, R., and G. D. Kinzer, 1949: The terminal velocity of fall for water droplets in stagnant air. *J. Meteor.,* **6,** 243–248.
Hauser, D., and P. Amayenc, 1981: A new method for deducing hydrometeor-size distributions and vertical air motions from Doppler radar measurements at vertical incidence. *J. Appl. Meteor.,* **20,** 547–555.
——, and ——, 1984: Raindrop size distributions and vertical air motions as inferred from zenith-pointing Doppler radar with the RONSARD system. *Radio Sci.,* **19,** 185–192.
Lhermitte, R. M., 1987: Observations of stratiform rain with 94 GHz and S-band Doppler radar. Air Force Geophysics Laboratory Tech. Rep. AFGL-TR-0268, 18 pp. [Available from Air Force Geophysics Laboratory, Air Force Systems Command, United States Air Force, Hanscom Air Force Base, MA 01731.]
——, 1988: Observations of rain at vertical incidence with a 94-GHz Doppler radar: An insight on Mie scattering. *Geophys. Res. Lett.,* **15,** 1125–1128.
——, 1990: Attenuation and scattering of millimeter wavelength radiation by clouds and precipitation. *J. Atmos. Oceanic Technol.,* **7,** 464–479.
Lohmeier, S. P., S. M. Sekelsky, J. M. Firda, G. A. Sadowy, and R. E. McIntosh, 1997: Classification of particles in stratiform clouds using the 33-GHz and 95-GHz polarimetric Cloud Profiling Radar System. *IEEE Trans. Geosci. Remote Sens.,* **35,** 256–270.
Marshall, J. S., and W. M. K. Palmer, 1948: The distribution of raindrops with size. *J. Meteor.,* **5,** 165–166.
Mead, J. B., A. L. Pazmany, S. M. Sekelsky, and R. E. McIntosh, 1994: Millimeter-wavelength radars for remotely sensing clouds and precipitation. *Proc. Inst. Electr. Eng.,* **82,** 1891–1906.
Mooradd, D. C., 1993: Design, development and construction of a dual-frequency, dual-polarized millimeter wave cloud profiling radar antenna. M.S. thesis, Dept. of Electrical and Computer Systems Engineering, University of Massachusetts, Amherst, MA, 69 pp. [Available from Physical Sciences and Engineering Library, Lederle Graduate Research Center, University of Massachusetts—Amherst, Amherst, MA 01003-4630.]
Probert-Jones, J. R., and W. G. Harper, 1961: Vertical air motion in showers as revealed by Doppler radar. *Proc. Ninth Weather Radar Conf.,* Kansas City, MO, Amer. Meteor. Soc., 23–26.
Rogers, R. R., 1964: An extension of the *Z–R* relation for Doppler radar. *Proc. 1964 World Conf. on Radio Meteorology Incorporating the Eleventh Weather Radar Conf.,* Boulder, CO, Amer. Meteor. Soc., 158–161.
——, and R. J. Pilié, 1962: Radar measurements of drop size distributions. *J. Atmos. Sci.,* **19,** 503–506.
——, D. Baumgardner, S. A. Ethier, D. A. Carter, and W. L. Ecklund, 1993: Comparison of raindrop size distributions measured by radar wind profiler and by airplane. *J. Appl. Meteor.,* **32,** 694–699.
Sekelsky, S. M., and R. E. McIntosh, 1996: Cloud observations with a polarimetric 33-GHz and 95-GHz radar. *J. Meteor. Atmos. Phys.,* **59,** 123–140.
Sekhon, R. S., and R. C. Srivastava, 1971: Doppler radar observations of drop size distributions in a thunderstorm. *J. Atmos. Sci.,* **28,** 983–994.
Tatarskii, V. I., 1971: *The Effects of the Turbulent Atmosphere on Wave Propagation.* NOAA TT 68-50464, 471 pp. [NTIS ISBN 07065 0680 4.]
Ulbrich, C. W., 1983: Natural variations in the analytical form of the raindrop size distribution. *J. Climate Appl. Meteor.,* **22,** 1764–1775.
Wakasugi, K. A., A. M. Matsuo, S. Fukao, and S. Kato, 1986: A direct method for deriving drop size distributions and vertical air velocities from VHF Doppler radar spectra. *J. Atmos. Oceanic Technol.,* **3,** 623–629.